

# An iterative method for the construction of N-body galaxy models in collisionless equilibrium

Denis Yurin<sup>1,2</sup> and Volker Springel<sup>1,2</sup>

<sup>1</sup>Heidelberg Institute for Theoretical Studies, Schloss-Wolfsbrunnenweg 35, 69118 Heidelberg, Germany

<sup>2</sup>Zentrum für Astronomie der Universität Heidelberg, ARI, Mönchhofstr. 12-14, 69120 Heidelberg, Germany

5 June 2018

## ABSTRACT

We describe a new iterative approach for the realization of equilibrium N-body systems for given density distributions. Our method uses elements of Schwarzschild’s technique and of the made-to-measure method, but is based on a different principle. Starting with some initial assignment of particle velocities, the difference of the time-averaged density response produced by the particle orbits with respect to the initial density configuration is characterized through a merit function, and a stationary solution of the collisionless Boltzmann equation is found by minimizing this merit function directly by iteratively adjusting the initial velocities. Because the distribution function is in general not unique for a given density structure, we augment the merit function with additional constraints that single out a desired target solution. The velocity adjustment is carried out with a stochastic process in which new velocities are randomly drawn from an approximate solution of the distribution function, but are kept only when they improve the fit. Our method converges rapidly and is flexible enough to allow the construction of solutions with third integrals of motion, including disk galaxies in which radial and vertical dispersions are different. A parallel code for the calculation of compound galaxy models with this new method is made publicly available.

**Key words:** stars: kinematics and dynamics – methods: numerical – galaxies: haloes – galaxies: kinematics and dynamics – galaxies: structure

## 1 INTRODUCTION

The large number of stars and dark matter particles in galaxies and galaxy clusters makes them essentially perfect collisionless systems. Their dynamics is hence described by the collisionless Boltzmann equation, coupled to self-gravity through Poisson’s equation. Relaxed systems correspond to stationary solutions of these equations, and much of the field of galactic dynamics is concerned with understanding different aspects of these solutions (see Binney & Tremaine 2008, for an excellent exposition). This is particularly important for using observational probes of kinematics to infer, for example, something about the underlying density distribution.

Numerical N-body simulations have become a primary workhorse to study collisionless systems, both in stationary and dynamic situations. Prominent examples include the study of bar instabilities (e.g. Athanassoula & Misiriotis 2002), the formation of spiral waves (e.g. D’Onghia et al. 2013), or major and minor mergers of galaxies (e.g. Barnes & Hernquist 1992; Hernquist & Mihos 1995). They are also actively used to study the response of disks to the bombardment by dark matter clumps (e.g. Kazantzidis et al. 2008; D’Onghia et al. 2010), or the radial migration of stars caused by resonance scattering (e.g. Sellwood & Binney 2002), and many more.

In carrying out numerical experiments targeting these ques-

tions, a recurrent challenge is to construct suitable initial conditions. One usually requires them to be in a reasonably stable, approximate equilibrium in the beginning, otherwise any subsequent dynamics may be dominated or heavily contaminated by the specific out-of-equilibrium state one started out with. Often, one has a relatively clear notion of the density structure one wants to realize, but initializing the particle velocities appropriately is a quite non-trivial problem. This is because doing this *perfectly* requires knowledge of the full distribution function (DF) of the system, or in other words, availability of a stationary solution of the collisionless Boltzmann equation. However, such solutions are analytically known only for a very limited number of density distributions.

There is hence significant demand to construct equilibrium solutions numerically, not only for realizing N-body initial conditions but also in the context of modelling observational data sets. In the latter case, finding such models is a main component of the reverse-engineering process aimed at constructing self-consistent three-dimensional systems that reproduce the observations. They can then be examined in great detail, allowing insights into properties that are not directly observable (Cretton et al. 1999; van den Bosch et al. 2012).

To our knowledge, there are presently mainly five different methods in use for constructing such equilibrium models:

arXiv:1402.1623v2 [astro-ph.CO] 19 Aug 2014

(i) DF-based: For certain mass distributions, the distribution function (DF) can be analytically calculated or accurately approximated. Unfortunately, this ideal case is not generally available for arbitrary density distributions. The main problem is that we do not know the analytical form of the third integral of motion. In some cases it may be reasonably approximated, but this leads at best to nearly self-consistent solutions (Kuijken & Dubinski 1995; Widrow & Dubinski 2005). Nevertheless, there are some useful classes of solutions known, for example for spherical galaxies (Ospkov 1979; Jaffe 1983; Merritt 1985; Hernquist 1990). However, because many real systems are not particularly close to any of these parameterized classes of systems, the approach is rather restrictive in practice.

(ii) Moment-based: Moments of the velocity distribution can be calculated or estimated with the hierarchy of Jeans equations. If one neglects higher order moments and assumes a functional form for the velocity distribution (often taken to be Gaussian, e.g. Hernquist 1993; Springel & White 1999) that reproduces the estimated moments, one obtains an approximate distribution function. This method is quite general and can be applied to all mass distributions. Since the true velocity distribution function is usually close to a triaxial Gaussian for much of the mass of a system, the method typically produces systems that are roughly in equilibrium. But the crux is that this equilibrium is by no means perfect, and that it is hard to overcome this limitation within this method. Especially difficult are the central regions of galaxies; when the constructed ICs are evolved in time, one here typically finds density ripples propagating through the system while it relaxes to a true equilibrium state. This can interfere with the interpretation of numerical experiments, especially when they require particularly quiet ICs.

(iii) Orbit-based method: Schwarzschild (1979) introduced a radically different approach to solve the problem. He suggested to integrate a wide variety of orbits in a given potential, and then to distribute the mass of the system over this orbit library such that the time-averaged density of the system becomes as close as possible to the one corresponding to the potential. Finding the weights of each of these orbits defines a linear optimization problem with positive coefficients, which can be solved iteratively. The resulting weights then effectively define the velocity distribution function. A practical problem with this method is that the size of the orbit library is severely constrained by the available memory. Moreover, the method is ill-conditioned in its basic form, something that needs to be cured by adding ad-hoc assumptions such as smoothness constraints or maximum entropy measures for the weights. Also, the velocity distribution functions constructed with this method are typically very noisy and may feature large jumps. One needs to smooth them, but the required level of smoothing is hard to define. Many attempts have been made to overcome these difficulties (e.g. Vandervoort 1984; Jalali & Tremaine 2011).

(iv) Made-to-measure: Attempts to improve on Schwarzschild's method have resulted in a new technique where the orbit integration process and the mass/weight redistribution are combined. This 'made-to-measure' technique makes the storage of a full orbit library unnecessary and therefore removes the memory barrier. But it still requires a smoothing procedure for the velocity distributions (Syer & Tremaine 1996; Dehnen 2009).

(v) Guided-relaxation: Another class of methods exploits the fact that any isolated system left to itself tends to an equilibrium state. Knowing the target mass distribution we may try to directly relax to it by steering a system appropriately in the process. This guiding can be done by introducing an additional force, e.g. adiabatic drag on the vertical components of the particle velocities in

order to squeeze the system (Holley-Bockelmann et al. 2001), or we may restrict particle mobility such that the target density distribution is maintained and the systems evolves towards a self-consistent equilibrium state (Rodionov et al. 2009). A disadvantage of this approach is that it involves one of the other methods to create an initial state for the further relaxation. Also, there is only limited control on the outcome, making it, e.g., difficult to construct systems with a prescribed velocity anisotropy.

The purpose of this article is to introduce a new, flexible approach for the construction of compound N-body models of axisymmetric galaxies in an essentially perfect equilibrium state. The method only requires the specification of the density profiles of the different components and a selection of the desired bulk properties of the velocity structure, such as the degree of rotational support or the ratio between radial and vertical velocity dispersion in the disk plane. Our code then constructs an N-body system that is in equilibrium and fulfills the imposed constraints on the velocity structure. Implicitly, it hence also provides a solution for the full 3D distribution function. This is achieved for essentially arbitrary axisymmetric density structure and by taking the mutual influence of different mass components (if present) fully into account. We argue that the resulting flexibility and accuracy makes our approach an attractive alternative compared with other IC generation methods in the literature.

This paper is structured as follows. In Section 2, we describe the basic methodology adopted in our method, which consists of an iterative procedure to adjust the velocities of an N-body realization of a galaxy model until the prescribed density structure is maintained self-consistently under time evolution, and the imposed velocity constraints are fulfilled. In Section 3, we highlight how we specify velocity constraints for different structural choices. They take the form of second velocity moments which we determine through solutions of the Jeans equations. We then specify in Section 4 various implementation details of our numerical methods as realized in the GALIC code introduced here. Section 5 is concerned with a brief description of the specific density profile models currently implemented in this code; these are employed for a suite of tests presented in Section 6. Finally, we conclude with a summary of our findings in Section 7.

## 2 METHODOLOGY

If density profiles for all collisionless mass components of a galaxy model are given, a random N-body realization of particle positions can be easily created by interpreting the density distribution as a probability field for a Poisson point process. But assigning suitable velocities to the particles is the difficult step. Our idea is to do this iteratively: Starting from some guess for the particle velocities, we try to correct them such that the system becomes closer to the desired equilibrium state. This is in some sense similar to Schwarzschild's method, where one models the distribution function from which the velocities are drawn through a set of weights, which are then iteratively adjusted until a global merit function is extremized. Differently from this technique, we however optimize the velocities of each particle directly. This eliminates the explicit orbit library of the Schwarzschild method, and all the restrictions that come with it. Instead, the particles of our N-body model themselves define the orbit set that is optimized. Importantly, this set is free of any discreteness restrictions or potential biases due to incompleteness of the Schwarzschild orbit library.

As basic merit function that is optimized we consider the difference between the target density field and the actual density response created by our  $N$ -body realization with the currently assigned initial velocities. The density response is here defined as the time-averaged density field of the  $N$ -body orbits, calculated in the static potential of the target density distribution. For a steady state system, this density response is supposed to be time invariant, and equal to the initial density field. We can readily imagine several different optimization schemes that adjust individual particle velocities iteratively such that this difference becomes as small as possible, for example multi-dimensional steepest decent.

Before discussing the details of our specific solution for this, it is however prudent to consider two apparent conceptual problems with the basic approach as outlined thus far. One is that the density structure does not uniquely specify the velocity structure of an equilibrium model, or in other words, there can be more than one steady-state solution of the collisionless Boltzmann equation for a given density structure. For example, for a spherically symmetric mass distribution, one can have solutions where the velocity distribution is isotropic everywhere, and the distribution function depends only on energy (the ‘ergodic’ case). But there are also solutions with an anisotropy between radial and tangential motions. Furthermore, one can also have many different axisymmetric solutions that feature different degrees of net rotation.

It is hence not clear to which equilibrium solution our adjustment scheme would converge when only the density response is optimized. This ambiguity can be lifted by making a selection for the desired type of solution one wants to obtain, and to suitably incorporate this constraint in the merit function. For example, one may request to obtain an anisotropic solution with a certain prescribed ratio of radial and tangential velocity dispersions. We can then augment our density based merit function with further conditions that enforce this velocity structure.

A second problem, of perhaps somewhat lesser importance, is the possibility of overfitting individual particle velocities. In the continuum limit of a collisionless system, individual particles are completed uncorrelated from each other. An iterative optimization approach will however always adjust a particle’s velocity given the current realization for positions and velocities of all other particles. This can in principle introduce undesired correlations between particles. Related to this, one may easily end up in an unfavorable local minimum of the merit function. We largely eliminate this effect by using a special optimization strategy in which new values for the velocity of a given particle are not searched in the vicinity of the current velocity, but rather globally in a random fashion, completely independent of the particle’s current velocity.

In the following, we first discuss our formalism for determining the density response of a particular realization and for measuring its goodness of fit through a merit function. We then extend the discussion to merit functions for the velocity moments, and present our approach for optimizing both of them concurrently.

## 2.1 Density merit function

Consider a collisionless  $N$ -body system with  $N$  particles, initial coordinates  $\hat{\mathbf{x}}_i$ , and initial velocities  $\hat{\mathbf{v}}_i$ . We assume that an initial density distribution  $\rho_0(\mathbf{x})$  is given, which can be used to create a realization of the coordinates  $\hat{\mathbf{x}}_i$  by random sampling. Determining the  $\hat{\mathbf{v}}_i$  is more complicated, however; we want to initialize them such that a stationary solution of the collisionless Boltzmann equation is obtained where the particles move in a given, stationary gravitational potential  $\Phi(\mathbf{x})$ . In other words, the collection of particles

should move such that the density field they create is time invariant and identical to the initial density distribution. If this is achieved, the gravitational field can then also be chosen self-consistently as the one created by the mass distribution itself (plus additional contributions by other mass distributions, if desired), such that one obtains a stationary self-gravitating solution of the Poisson-Vlasov system.

The density field created by the particles of our system can be formally expressed through a superposition of Dirac delta functions:

$$\rho(\mathbf{x}, t, \hat{\mathbf{v}}_1, \dots, \hat{\mathbf{v}}_N) = \sum_{i=1}^N m_p \delta(\mathbf{x}_{\text{orbit}}(\hat{\mathbf{x}}_i, \hat{\mathbf{v}}_i, t) - \mathbf{x}), \quad (1)$$

where the function  $\mathbf{x}_{\text{orbit}}(\hat{\mathbf{x}}', \hat{\mathbf{v}}', t)$  describes the time-dependent orbit of a particle starting in the phase-space point  $(\hat{\mathbf{x}}', \hat{\mathbf{v}}')$ . Note that in the expression for the density field we have explicitly retained the dependence on the initial values of the particles velocities (which we have yet to determine), whereas the initial positions can be viewed as fixed parameters.

Next, we define the time-averaged density response for the chosen initial velocities as

$$\bar{\rho}(\mathbf{x}, \hat{\mathbf{v}}_1, \dots, \hat{\mathbf{v}}_N) = \lim_{T \rightarrow \infty} \frac{1}{T} \int_0^T \rho(\mathbf{x}, t, \hat{\mathbf{v}}_1, \dots, \hat{\mathbf{v}}_N) dt. \quad (2)$$

The best steady-state for the system can be defined as the smallest possible difference between the time-averaged density and the initial density field. To this end, we introduce an objective function

$$S(\hat{\mathbf{v}}_1, \dots, \hat{\mathbf{v}}_N) = \int |\bar{\rho}(\mathbf{x}, \hat{\mathbf{v}}_1, \dots, \hat{\mathbf{v}}_N) - \rho_0(\mathbf{x})| d\mathbf{x}, \quad (3)$$

which measures the  $L_1$ -norm of the difference between the two fields. The linear weighting of the mass difference at a given location is motivated by the source term in Poisson’s equation, which is ultimately what we want to keep constant as much as possible in a steady state to avoid potential fluctuations that can modify particle energies.

Therefore, the task to construct a best possible steady-state that has a given density distribution is primarily about finding the  $\hat{\mathbf{v}}_i$  such that the difference  $S$  defined by equation (3) reaches a minimum. Note that this can in principle be viewed as a high-dimensional minimization problem with respect to the initial velocities. This could, for example, be tackled with the method of steepest decent. A direct adjustment of the velocities to minimize the function  $S$  is indeed the central idea we pursue in this paper, yielding a novel scheme for constructing equilibrium solutions. There are however a number of obstacles that make such a minimization non-trivial.

First of all, the problem needs to be somehow discretized, otherwise we cannot meaningfully define a density field for a finite number of particles. We will deal with this aspect in the remainder of this subsection. A further conceptual problem, namely the non-uniqueness of the obtained solutions, needs to be addressed as well.

Let’s assume we discretize the space covered by our system in terms of cells of volume  $V_j$ , indexed by  $j$ . The cells cover the volume but they do not need to be of the same size (e.g. we may choose to use adaptive logarithmic grids, as we do in practice). The merit function (3) can now be written as

$$S(\hat{\mathbf{v}}_1, \dots, \hat{\mathbf{v}}_N) = \sum_j |\bar{M}_j(\hat{\mathbf{v}}_1, \dots, \hat{\mathbf{v}}_N) - M_j^0|, \quad (4)$$

where  $\bar{M}_j$  and  $M_j^0$  give the masses of the time-averaged and the

initial density field that fall into cell  $j$ , respectively. To determine  $\bar{M}_j$ , we add the time-averaged contributions of the orbits of all particles to this spatial cell. Since the trajectories of different points require different times to saturate their impact on the common averaged density, it is computationally more efficient to follow their orbits over individually chosen time scales  $T_i$ . We can then write

$$\bar{M}_j = \sum_{i=1}^N \int_{\text{cell } j} d\mathbf{x} \int \frac{dt}{T_i} m_p \delta(\mathbf{x}_{\text{orbit}}(\hat{\mathbf{x}}_i, \hat{\mathbf{v}}_i, t) - \mathbf{x}). \quad (5)$$

This reduces to

$$\bar{M}_j = \sum_{i=1}^N m_p \tau_j^{\text{orbit}}(\hat{\mathbf{x}}_i, \hat{\mathbf{v}}_i), \quad (6)$$

where  $\tau_j^{\text{orbit}}(\hat{\mathbf{x}}_i, \hat{\mathbf{v}}_i)$  gives the fraction of time an orbit starting in the given phase-space point spends in cell  $j$ . The expected mass in the cell,  $M_j^0$ , is simply given by

$$M_j^0 = \int_{\text{cell } j} \rho_0(\mathbf{x}) d\mathbf{x}. \quad (7)$$

We note that the above equations correspond to so-called nearest grid point assignment of the current position of a particle to the mesh. One can replace this with a higher-order assignment scheme if desired, with the simplest possibility being clouds-in-cell assignment<sup>1</sup>.

A more important question concerns the choice of the spatial binning scheme. There should be enough bins to resolve all relevant detail of the density distribution, but the Poisson noise affecting  $\bar{M}_j$  due to the finite number of particles we use clearly limits the minimum size of a bin that is reasonable. In order to make the noise in each bin comparable, it is advantageous to choose the bins sizes such that they contain roughly equal mass. We follow this strategy by adopting a hierarchical adaptive binning scheme combined with a logarithmic grid. We will describe this approach in full detail in Section 4.1.

## 2.2 Velocity dispersion merit functions

As we discussed earlier, the requirement of a stationary density field does not in general imply a unique solution for the distribution function. For example, in an axisymmetric system, it would always be possible to flip the signs of the azimuthal velocities to generate, e.g., a system where all particles orbit around the  $z$ -axis with positive  $L_z$ , or with negative  $L_z$ , or with any desired mixture of the two. It is hence unclear in which minimum one ends up when one would try to directly minimize  $S$  with respect to the  $\hat{\mathbf{v}}_i$ .

In order to lift this ambiguity and make the solution more well defined, we need to add additional constraints that drastically reduce the acceptable solution space. We do this by invoking symmetry assumptions about the velocity structure of the system. This then allows solving the Jeans equations for the second velocity moments, which we impose as a further optimization constraint.

In general, there are three first moments and three second (reduced) moments of the velocity distribution function at every point. We will here focus on axisymmetric systems and employ cylindrical coordinates  $(R, \phi, z)$ . In a stationary system, we always have  $\langle v_R \rangle = 0$  and  $\langle v_z \rangle = 0$ . We shall now assume that as part of specifying our desired target system, we provide enough assumptions

such that the three dispersions and the azimuthal streaming can be calculated everywhere, i.e.  $\sigma_R^2 = \langle v_R^2 \rangle$ ,  $\sigma_\phi^2 = \langle (v_\phi - \bar{v}_\phi)^2 \rangle$ ,  $\sigma_z^2 = \langle v_z^2 \rangle$ , and the mean azimuthal streaming  $\bar{v}_\phi = \langle v_\phi \rangle$  can be considered to be known as a function of  $(R, z)$ . How we compute these quantities in practice for different cases will be discussed in Section 3.

In order to impose these velocity moments as additional constraints on the initial velocities  $\hat{\mathbf{v}}_i$ , we again consider spatial bins indexed by  $j$ , allowing us to estimate the actual (initial) velocity dispersions of our particular realization. For example, the average radial dispersion in bin  $j$  is given by

$$[\sigma_R^2]_j^{\text{actual}} = \frac{1}{M_j} \sum_{\hat{\mathbf{x}}_i \text{ in cell } j} m_p (\hat{\mathbf{v}}_i \cdot \mathbf{e}_R^{(i)})^2. \quad (8)$$

The normalization factor

$$M_j = \sum_{\hat{\mathbf{x}}_i \text{ in cell } j} m_p \quad (9)$$

is simply equal to the mass of the initial realization that falls into the spatial bin. The vector  $\mathbf{e}_R^{(i)}$  is the radial unit vector at the position of particle  $i$ . The expected target velocity dispersion in the bin is given by

$$[\sigma_R^2]_j^{\text{target}} = \frac{1}{M_j^0} \int_{\text{cell } j} \rho_0(\mathbf{x}) \sigma^2(\mathbf{x}) d\mathbf{x}, \quad (10)$$

where  $M_j^0$  is the mass expected in the continuum in the cell. We may then define a merit function that measures the deviation of the actually realized velocity dispersion relative to the target value. To this end we adopt

$$Q_R = \sum_j \frac{|[\sigma_R^2]_j^{\text{actual}} - [\sigma_R^2]_j^{\text{target}}|}{[\sigma_R^2]_j^{\text{target}}}. \quad (11)$$

Similarly, we define merit functions  $Q_z$  and  $Q_\phi$  for the dispersions in the  $z$ -direction and the azimuthal  $\phi$ -direction, respectively. In the azimuthal direction, we actually measure and constrain both the full second moment  $\langle v_\phi^2 \rangle$  and the dispersion relative to the mean streaming  $\sigma_\phi^2$ . Combined, this then also constrains the mean streaming itself.

As for the density case, we need to adopt a suitable discretization for the spatial bins. In order to avoid biases due to different noise levels in the bins, we adopt bins in which the mass per bin (or, equivalently, the number of particles) is roughly constant, a situation we realize with the help of a hierarchical adaptive binning scheme. We note that it is possible to employ the same spatial bins as used for the density merit function, but if desired the corresponding target value for the mass per bin can also be chosen differently.

## 2.3 Optimization procedure

Our goal is to iteratively adjust the  $\hat{\mathbf{v}}_i$  such that  $S$ ,  $Q_R$ ,  $Q_\phi$  and  $Q_z$  are simultaneously minimized. We do this by combining these quantities into a single goodness-of-fit parameter,

$$S_{\text{global}} = S + \chi(Q_R + Q_\phi + Q_z), \quad (12)$$

where the constant  $\chi$  is adjusted such that  $S$  and  $Q_R + Q_\phi + Q_z$  are of the same magnitude and have the same units. In other words, we give equal weight to the density and velocity constraints.

The function  $S_{\text{global}}(\hat{\mathbf{v}}_1, \dots, \hat{\mathbf{v}}_N)$  depends only on the initial particle velocities. Hence we are formally charged with the task to find its minimum in the high-dimensional space of all the  $3N$

<sup>1</sup> We actually use the latter in our implementation, even though the improvement relative to nearest grid point assignment is here minor.

velocity components. Trying to find this minimum is a computationally rather tricky problem, because the function will feature a large number of local minima in which a direct search may easily get stuck. Also, the function is non-linear and expensive to evaluate – calculating  $S$  involves orbit integrations of a large number of particles over a long time interval. Even if a single force calculation is comparatively cheap due to the static potential, the cumulative CPU cost can become demanding, especially since we are not dealing just with a single particle but rather with a (potentially quite large) particle collection of size  $N$ .

Nevertheless, it is still possible to estimate the local gradient of  $S_{\text{global}}$  with respect to the  $\hat{\mathbf{v}}_i$  and then to move in the direction of steepest decent by simultaneously modifying all velocities in the direction opposite to the gradient. But finding a local minimum in this way will still be very hard (we have tried); typically, one will instead overshoot in at least one of the many dimensions of the problem.

Another consideration also argues against this brute force approach. Physically, we expect that the particles should be completely uncorrelated in proper collisionless initial conditions. Directly minimizing  $S_{\text{global}}$  simultaneously with respect to all velocities invokes the danger of ‘overfitting’, where a low value of the merit function is obtained through the introduction of velocity correlations in the specific  $N$ -body realization of the system.

Our solution to these problems involves two components. First, we serialize the minimization procedure, i.e. we always pick only one particle randomly, and then optimize its velocity such that  $S_{\text{global}}$  is reduced. Second, we do not actually try to adjust the velocity of the single particle such that  $S_{\text{global}}$  is necessarily minimized, as may be done by using the result of a line search along a single parameter. Rather, we simply randomly pick a new guess for the particle’s velocity and (re)evaluate the merit function for this choice. If the proposed velocity improves the fit, we retain it as the new velocity of the particle, otherwise we simply keep the particle’s old velocity and proceed with the next particle. This is simply repeated until the fit cannot be improved significantly any more. We note that this approach bears some resemblance to Monte Carlo Markov Chain techniques, except that we are here trying to find a global optimum rather than exploring a likelihood surface where one also moves occasionally away from the optimum with a certain probability.

The distribution from which one draws the trial velocities is in principle arbitrary, provided it is broad enough to sample all allowed velocities. However, it is highly advantageous to make it close to the target distribution function, because in this case the convergence speed can be expected to be particularly rapid (just as in MCMC). In our case, we can simply use Gaussians for that, as we already have the second moments in hand based on our Jeans solutions and the distribution function will in most cases resemble a Gaussian locally, so this should facilitate rapid convergence. Note that every new trial velocity we pick is completely independent of the previous value, as well as of the velocities of all other particles. This helps to minimize correlations between different particles in the created initial conditions, and it prevents to get easily stuck in a local minimum. Nevertheless, velocity correlations are not completely absent, because the acceptance decision for the velocity of a particular particle still depends on the discrete spectrum of velocities realized at this instant for all the other particles. But as our results show, any present residual correlations do not seem to negatively impact the quality of the created initial conditions.

In practice, we choose to process all particles in a random order. In each pass over the particles, we pick for a given particle one

of its three principal coordinate directions and draw a random trial value for the corresponding velocity component. We note that the evaluation of  $S_{\text{global}}$  can be significantly accelerated if only one particle is varied. In this case, only the summed orbital response of all particles needs to be stored, without requiring storage of all the responses individually. Evaluating  $S_{\text{global}}$  for a changed velocity of one particle then boils down to calculating the orbit response for this particle twice, both for the old and new velocities. The differential between the two results can then be appropriately added to the global response to assess the change in  $S_{\text{global}}$ .

### 3 VELOCITY CONSTRAINTS

As discussed above, a problematic aspect of optimizing only a density merit function is that it is ambiguous to which solution this will converge. Recall that for a given density distribution there will in general be a vast number of possible distribution functions. The iterative optimization will yield a particular realization of one of these distribution functions, and this solution might depend on the initial velocity guesses one has used at the beginning. In order to make the solution well defined, we need to impose additional constraints that reflect the desired properties of the specific solution one is looking for. We do this in terms of second moments of the velocity distribution and by forcing the system to converge to a solution that features these moments. The moments themselves are calculated from the Jeans equations. Different possibilities for a specification of the desired properties of the target system exist.

#### 3.1 Spherically symmetric distribution functions

If the density structure is spherically symmetric and the velocity distribution function depends at most on the magnitude of the angular momentum, we can make use of the spherically symmetric Jeans equation for the second radial velocity moment,

$$\frac{\partial(\rho\sigma_r^2)}{\partial r} + 2\frac{\beta\rho\sigma_r^2}{r} + \rho\frac{\partial\Phi}{\partial r} = 0. \quad (13)$$

Here  $\sigma_r^2 = \langle v_r^2 \rangle$  is the radial dispersion. The velocity distribution functions in the transverse directions at any given position need not be equal to that in the radial direction, but we have  $\sigma_\theta = \sigma_\phi$  due to the assumed symmetry. The degree of radial–tangential anisotropy is usually measured in terms of

$$\beta = 1 - \frac{\sigma_t^2}{2\sigma_r^2} = 1 - \frac{\sigma_\phi^2}{\sigma_r^2}, \quad (14)$$

where  $\sigma_t^2 = \sigma_\theta^2 + \sigma_\phi^2 = 2\sigma_\theta^2$  measures the total tangential dispersion, and due to spherical symmetry we have  $\sigma_\theta = \sigma_\phi$ . If the distribution is isotropic, we have  $\beta = 0$ . If the orbits are biased towards radial motions we have  $\beta > 0$ , while for  $\beta < 0$  they are preferentially tangential.

For given  $\rho(r)$  and prescribed  $\beta(r)$ , and thanks to the purely radial dependence, equation (13) becomes an ordinary differential equation for  $\rho\sigma_r^2$  which can be readily integrated using the boundary condition  $\rho\sigma_r^2 = 0$  for large radii. Dividing the solution by the density then yields the dispersion  $\sigma_r^2(r)$  as a function of radius, and from it we also obtain  $\sigma_\theta^2(r) = (1 - \beta)\sigma_r^2(r)$ .

We note that we may choose  $\beta$  to be a function of radius, as suggested by the structure measured for cosmological dark matter halos. Hansen & Moore (2006) found that the local anisotropy of dark matter halos correlates well with the logarithmic slope

$$\alpha = \frac{d \ln \rho}{d \ln r} \quad (15)$$

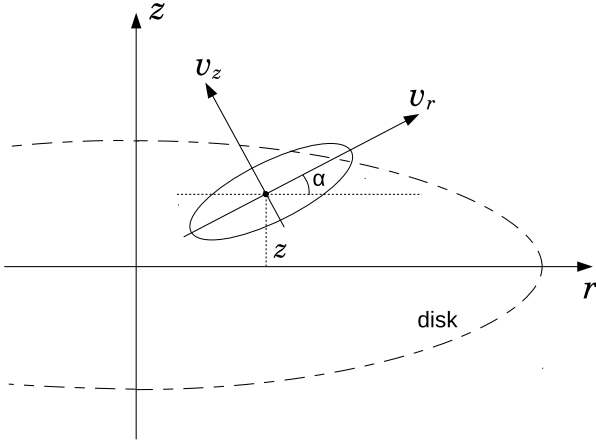


**Figure 1.** Sketch of the geometry adopted to describe the assumed tilt of the velocity ellipsoid in the  $f(E, L_z, I_3)$  case.

of the density profile. Their numerical results are well fit by the relation

$$\beta(r) = -0.15 - 0.2\alpha, \quad (16)$$

which we adopt as an additional option in our IC code. This implies nearly isotropic orbits in the center of a Hernquist or NFW halo, and a growing preference for more radial dispersion as a function of distance.

A particularly simple choice for  $\beta(r)$  is the isotropic case,  $\beta = 0$ , where the velocity distribution function is independent of direction at every point. In this ergodic case, the distribution function depends only on energy. Hernquist (1990) constructed such a solution for a density profile of the form  $\rho(r) \propto r^{-1}(r+a)^{-3}$ , which is cosmologically particularly relevant as it has a shape similar to the NFW density profile (Navarro et al. 1997) measured for relaxed halos in cold dark matter structure formation simulations. This makes the isotropic Hernquist model a particularly useful analytic distribution, and we will also use it here to verify our procedures. We note however that a yet more realistic model would be one with a radially varying anisotropy  $\beta(r)$ . No analytic distribution functions are known for this case, but such models can be readily constructed with our new method.

### 3.2 Axisymmetric systems with two integrals of motion

For axisymmetric systems, the angular momentum  $L_z$  around the  $z$ -axis is a conserved quantity for all orbits, hence we expect the distribution function to depend on  $L_z$  besides energy  $E$ . In general, there can be a third integral of motion,  $I_3$ , which is however often not easy to identify and therefore considered “non-classical”. If one disregards  $I_3$  and assumes that the distribution function is only a function of  $E$  and  $L_z$ , then the situation simplifies considerably, as one can then infer that all mixed moments of the velocity distribution vanish (i.e.  $\langle \sigma_R \sigma_z \rangle = 0$ ). In this case the axisymmetric Jeans equations simplify considerably and can be comparatively easily solved.

With two integrals of motion, the non-trivial axisymmetric Jeans equations become:

$$\frac{\partial(\rho\sigma_z^2)}{\partial z} + \rho \frac{\partial\Phi}{\partial z} = 0, \quad (17)$$

and

$$\langle v_\phi^2 \rangle = \sigma_R^2 + \frac{R}{\rho} \frac{\partial(\rho\sigma_R^2)}{\partial R} + R \frac{\partial\Phi}{\partial R}. \quad (18)$$

The mean streaming motions in the radial and vertical directions vanish,  $\langle v_R \rangle = \langle v_z \rangle = 0$  (but not necessarily in the azimuthal direction), and importantly, the radial and vertical dispersions are equal everywhere,  $\sigma_R^2 = \sigma_z^2$ .

This in particular means that the density distribution fully specifies the vertical and radial dispersions in the meridional plane  $(R, z)$ . They can be explicitly calculated as

$$\sigma_R^2 = \sigma_z^2(R, z) = \frac{1}{\rho(R, z)} \int_z^\infty \rho(z', R) \frac{\partial\Phi}{\partial z}(R, z') dz'. \quad (19)$$

Once these dispersions are known, we can now determine the second moment  $\langle v_\phi^2 \rangle$  of the azimuthal motion from the radial Jeans equation (18). However the mean streaming  $\langle v_\phi \rangle$  in the azimuthal direction is not specified by the Jeans equations. Indeed,  $\langle v_\phi \rangle$  does not have to be zero if there is net rotation. For any given solution with non-zero  $\langle v_\phi \rangle$ , one can readily construct new, equally valid equilibrium solutions, for example by reversing all or a fraction of the particles’  $\phi$ -motions. It is hence clear that the requirement of axisymmetry does not specify  $\langle v_\phi \rangle$ . In fact, we are (within limits) free to set this.

We adopt the parameterization

$$\langle v_\phi \rangle^2 = k^2 [\langle v_\phi^2 \rangle - \sigma_R^2] \quad (20)$$

suggested by Satoh (1980) to specify the mean streaming. For the interesting choice  $k = 1$ , we obtain for the azimuthal dispersion

$$\sigma_\phi^2 \equiv \langle v_\phi^2 \rangle - \langle v_\phi \rangle^2 = \sigma_R^2 = \sigma_z^2, \quad (21)$$

i.e.  $\sigma_\phi^2$  is then equal to the radial and vertical dispersions. This defines the case of an isotropic rotator. But we may also adopt a lower or higher value for  $k$ , or even one with a spatial dependence, up to the maximum allowed local value of

$$k_{\max}^2 = \frac{\langle v_\phi^2 \rangle}{\langle v_\phi^2 \rangle - \sigma_R^2}. \quad (22)$$

In  $k$  climbs up to this value, the azimuthal dispersion vanishes and we have  $\langle v_\phi \rangle^2 = \langle v_\phi^2 \rangle$ , corresponding to a system with the maximum possible angular momentum for a given density structure. In our GALIC code, we either choose a constant  $k$  or specify  $k$  in units of  $k_{\max}$  when the case of a  $f(E, L_z)$  distribution function is selected.

### 3.3 General systems with three integrals of motion

While simple disk models can be constructed as isotropic rotators, observations in the Milky Way at the Solar circle suggest that  $\sigma_R$  is not equal to  $\sigma_z$ . Rather, the two dispersions are related approximately by  $\sigma_z \simeq 0.5 \sigma_R$  (Binney & Merrifield 1998). Even if the Milky Way can still be described well as an axisymmetric system, this already means that the distribution function is not only dependent on  $(E, L_z)$ ; instead, a third integral of motion must play an important role. In the outer parts of the disk, this is approximately given by the energy of the vertical motion in the disks potential, but in the inner parts of the disk this identification presumably becomes a poor approximation.

Another interesting observational fact is that the velocity ellipsoid above the disk mid plane is not aligned with the coordinate plane; instead, it appears tilted (i.e.  $\langle v_R v_z \rangle \neq 0$ ) towards the centre

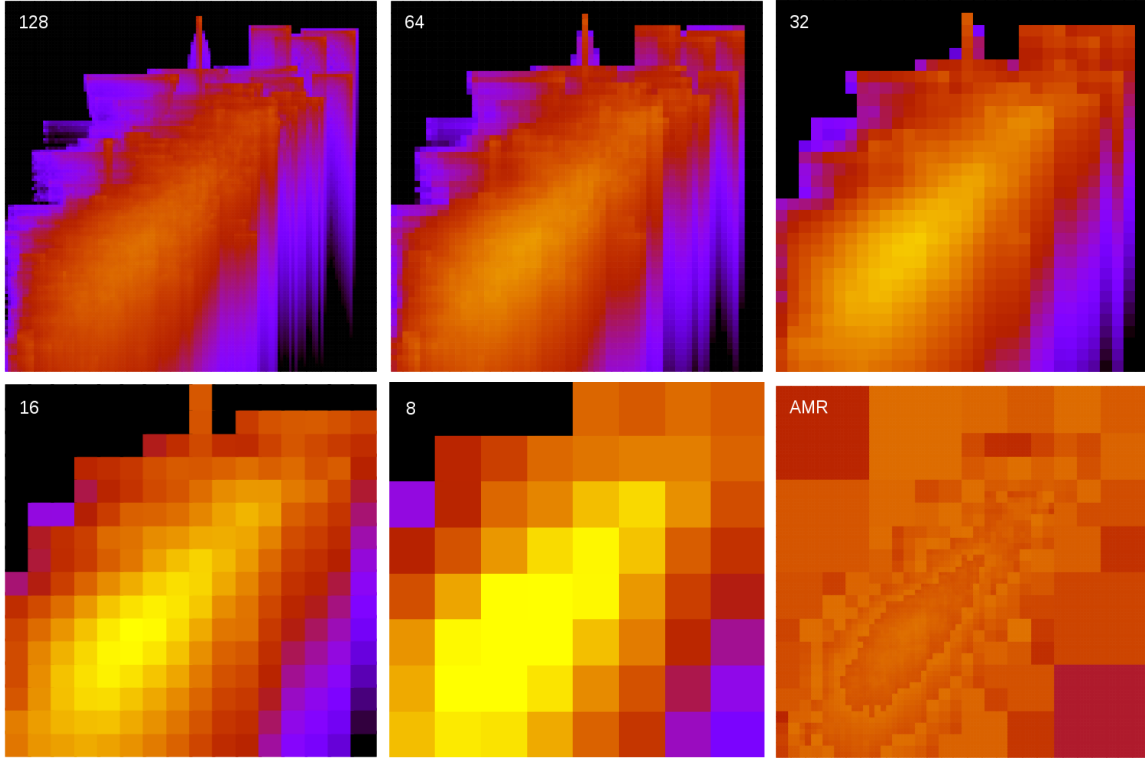


**Figure 2.** Density response of our hierarchical binning scheme. The top left panel shows the average orbit response as recorded on the finest grid used (which is a logarithmic grid with  $256^2$  pixels). The next four panels show coarsened representations of this field, with resolutions of  $64^2$  to  $8^2$  pixels (this continues to even coarser meshes that are not shown). Finally, the bottom right panel shows the variable resolution response that is actually used to compare with the target density distribution, based on bins containing roughly equal mass.

| Model | Components and their shape   | Imposed velocity structure   |
|-------|--|--|
| H1    | spherical dark halo  | ergodic (i.e. isotropic Hernquist model)   |
| H2    | spherical dark halo  | spherical anisotropy, radial orbits dominating, $\beta = 0.5$  |
| H3    | spherical dark halo  | spherical anisotropy, tangential orbits dominating, $\beta = -1.0$                                     |
| H4    | spherical dark halo  | radially varying anisotropy, $\beta(r) = -0.15 - 0.20 \frac{d \log \rho}{d \log r}$                    |
| H5    | spherical dark halo  | axisymmetric velocity structure, isotropic rotator with $k = 1$  |
| H6    | prolate dark halo with $s = 0.85$                                  | axisymmetric velocity structure, no net rotation   |
| H7    | oblate dark halo with $s = 1.15$                                   | axisymmetric velocity structure, no net rotation   |
| B1    | spherical dark halo, spherical bulge                               | ergodic  |
| B2    | spherical dark halo, spherical bulge                               | different anisotropies for bulge and halo, $\beta_{\text{halo}} = 0.5$ , $\beta_{\text{bulge}} = -1.0$ |
| B3    | prolate dark halo $s = 0.85$ , spherical bulge                     | axisymmetric velocity structure, no net rotation   |
| B4    | oblate dark halo $s = 1.15$ , prolate bulge $s = 0.85$             | axisymmetric velocity structure, no net rotation   |
| D1    | spherical dark halo, thin disk                                     | axisymmetric velocity structure for halo and disk, disk isotropic rotator                              |
| D2    | prolate dark halo with $s = 0.85$ , thin disk                      | axisymmetric velocity structure for halo and disk, disk isotropic rotator                              |
| D3    | spherical dark halo, thin disk                                     | disk with $f(E, L_z, I_3)$ structure and $f_R = 2.0$ , halo axisymmetric with $k = 0$                  |
| D4    | spherical dark halo, thin disk                                     | disk with $f(E, L_z, I_3)$ and $f_{R,\text{disk}} = 4.0$ , halo axisymmetric with $k = 0.5$            |
| D5    | prolate dark halo with $s = 0.85$ , thin disk                      | disk with $f(E, L_z, I_3)$ and $f_{R,\text{disk}} = 2.0$ , halo axisymmetric isotropic rotator         |
| M1    | spherical dark halo, spherical bulge, thin disk                    | axisymmetric structure for halo and bulge (no rotation), disk isotropic rotator                        |
| M2    | spherical dark halo, spherical bulge, thin disk                    | axisymmetric velocities for halo/bulge, disk with $f(E, L_z, I_3)$ , $f_{R,\text{disk}} = 2.0$         |
| M3    | spherical dark halo, spherical bulge, thin disk                    | disk with $f(E, L_z, I_3)$ and $f_R = 4.0$ , bulge no rotation, halo with $k = 0.1$                    |
| M4    | prolate dark halo $s = 0.85$ , oblate bulge $s = 1.15$ , thin disk | disk with $f(E, L_z, I_3)$ , $f_R = 2.0$ , halo and bulge both isotropic rotators                      |

**Table 1.** Set of basic galaxy models constructed for testing purposes with the methods outlined in this paper. Unless stated otherwise, we have used  $10^6$  particles for each model component. The models labeled ‘H1’, ‘H2’, etc., contain only a dark matter halo but differ in the halo shape or the assumptions made for the velocity structure. The models denoted ‘B1’, ‘B2’, and so on, contain a bulge in addition to the halo, and the modes with ‘D1’, ‘D2’, etc., feature a disk in addition to the halo. Finally the models ‘M1’, ‘M2’, etc., contain both a stellar bulge and a stellar disk, next to a dark matter halo.

of the system. Using RAVE velocity data, Siebert et al. (2008) and Binney et al. (2014) quantified the tilt at 1 kpc above the disk to be around  $\alpha = 7^\circ$  (see sketch of Fig. 1). We are hence forced to apply the general axisymmetric Jeans equations, which take the form:

$$\frac{\partial(\rho\sigma_z^2)}{\partial z} + \rho \frac{\partial\Phi}{\partial z} + \frac{1}{R} \frac{\partial(R\rho\langle v_R v_z \rangle)}{\partial R} = 0, \quad (23)$$

$$\langle v_\phi^2 \rangle = \sigma_R^2 + \frac{R}{\rho} \frac{\partial(\rho\sigma_R^2)}{\partial R} + R \frac{\partial\Phi}{\partial R} + \frac{R}{\rho} \frac{\partial(\rho\langle v_R v_z \rangle)}{\partial R}, \quad (24)$$

$$\frac{\partial(\rho\langle v_z v_\phi \rangle)}{\partial z} + \frac{1}{R^2} \frac{\partial(R^2\rho\langle v_R v_\phi \rangle)}{\partial R} = 0. \quad (25)$$

This system of equations is significantly under-specified and additional assumptions are needed for closure. We shall assume that the velocity ellipsoid is not tilted in the  $\phi$ -direction, hence  $\langle v_z v_\phi \rangle = \langle v_R v_\phi \rangle = 0$ . This eliminates the third equation. However, we need to retain a tilt in the meridional plane, as encoded by  $\langle v_R v_z \rangle$ . If  $\alpha$  is the local angle between the velocity ellipsoid and the  $R$ -axis, this mixed moment can be expressed in terms of the radial and vertical moments, i.e. we have

$$\langle v_R v_z \rangle = \frac{1}{2} \tan(2\alpha) [\sigma_R^2 - \sigma_z^2]. \quad (26)$$

For reference, the dispersions in the rotated coordinate frame  $(R', z')$  are given by

$$\langle v_{R'}^2 \rangle = \sigma_R^2 \cos^2(\alpha) + \langle v_R v_z \rangle \sin(2\alpha) + \sigma_z^2 \sin^2(\alpha), \quad (27)$$

$$\langle v_{z'}^2 \rangle = \sigma_R^2 \sin^2(\alpha) - \langle v_R v_z \rangle \sin(2\alpha) + \sigma_z^2 \cos^2(\alpha). \quad (28)$$

The tilt angle is the one for which  $\langle v_{R'} v_{z'} \rangle = 0$ , by construction.

Interestingly, the tilt observed for the Galaxy at the Solar circle is consistent with the velocity ellipsoid pointing approximately to the center of the Galaxy; the most recent determination by Binney et al. (2014) gives  $\alpha \sim 0.8 \arctan(z/R)$ . We here assume for definiteness that this alignment is perfect and holds throughout the system, in which case the angle  $\alpha$  is simply given by

$$\tan \alpha = \frac{z}{R}. \quad (29)$$

Specifying the orientation of the velocity ellipsoid in this way has the nice property of naturally producing a spherically symmetric orientation close to the galactic centre, i.e. the ‘disk regime’ seamlessly transitions to a ‘bulge regime’. Far out in a thin disk, the velocity ellipsoid will align with the coordinate axes, while near to the centre the situation becomes closer to that in a spherically symmetric case with a radial alignment, which seems plausible.

Prescribing the tilt angle is not yet enough to solve equations (23) and (24), because they involve four unknowns. An additional assumption is required. To this end, we adopt a prescribed relation between the radial and vertical dispersions in the tilted velocity ellipsoids, namely

$$\langle v_{R'}^2 \rangle = f_R \langle v_{z'}^2 \rangle, \quad (30)$$

where  $f_R$  is a factor specifying the anisotropy between radial and transverse motions. For the disk of a Milky Way like galaxy, we would expect  $f_R \simeq 2$  at the Solar circle, but little is known about a potential radial variation of this value. We also note in passing that the Toomre stability criterion depends sensitively on  $\sigma_R$ , so invoking values  $f_R > 1$  is one way of stabilizing a stellar disk of given thickness against axisymmetric perturbations. For simplicity, we shall assume a spatially constant value for  $f_R$  in the disk, but

note that our techniques could be easily generalized to include a radial or vertical variation of this factor.

Given the above model for the dispersions, we can now express the mixed moment  $\langle v_R v_z \rangle$  through the vertical dispersion, namely

$$\langle v_R v_z \rangle = h \sigma_z^2, \quad (31)$$

where the function  $h = h(R, z)$  is given by

$$h = \frac{(f-1) \tan(2\alpha)}{2 \cos^2(\alpha) - 2f \sin^2(\alpha) + (1+f) \sin(2\alpha) \tan(2\alpha)}, \quad (32)$$

and the shortcut  $f = f_R$  is understood. The Jeans equation (23) now becomes an inhomogenous first order partial differential equation (PDE) for  $\sigma_z^2$ . Defining  $q \equiv \rho\sigma_z^2$ , the relevant equation takes the form

$$\frac{\partial q}{\partial z} + \frac{\partial(hq)}{\partial R} + \frac{hq}{R} + \rho \frac{\partial\Phi}{\partial z} = 0. \quad (33)$$

We can solve this PDE numerically with the methods of lines by discretizing in  $R$  and replacing the spatial  $R$ -derivative with a finite difference approximation. We can then integrate the resulting system of coupled ordinary differential equations along the  $z$ -direction, starting at  $z \simeq \infty$  and ending up at  $z = 0$ . The initial condition is  $q(R, z = \infty) = 0$ , augmented with the boundary condition  $q(R = \infty, z) = 0$ . For numerical stability, one needs to take care that an upwind finite difference estimate for the  $R$ -derivative is used. Note also that the  $hq/R$  term is not singular for  $R = 0$ , because  $h/R \rightarrow (f-1)/f$  for  $R \rightarrow 0$ .

Having obtained a solution for  $q(R, z)$ , we then readily have  $\sigma_z, \sigma_R^2, \langle v_R v_z \rangle$ , as well as  $\langle v_{R'}^2 \rangle$  and  $\langle v_{z'}^2 \rangle$  throughout the meridional plane. Similar as with the axisymmetric  $f(E, L_z)$  case, we still have the freedom to choose a streaming velocity in the  $\phi$ -direction, except that now we have to use equation (24) to infer the corresponding dispersion available in the azimuthal direction. We continue to use the parametrization of equation (21) for the azimuthal streaming. For the case  $k = 1$ , we then get  $\sigma_\phi^2 = \sigma_R^2$  in the mid-plane.

We note that one can also obtain from epicycle theory a statement about the relation between  $\langle (v_\phi - v_c)^2 \rangle$  and  $\sigma_R^2$ , valid for small radial dispersions  $\sigma_R$ , namely

$$\frac{\langle (v_\phi - v_c)^2 \rangle}{\sigma_R^2} \simeq \frac{1}{\gamma^2} \quad (34)$$

where  $\gamma = 2\Omega/\kappa$ .  $\Omega^2 = \frac{1}{R} \frac{\partial\Phi}{\partial R}$  is the circular orbit frequency, and

$$\kappa^2 = R \frac{d\Omega^2}{dR} + 4\Omega^2 \quad (35)$$

is the epicycle frequency. Typically we have  $1/\gamma^2 \simeq 0.5$ . We note that equation (34) is only reliable for very cold thin disks, with  $\sigma_R \ll v_c$  (see Binney & Tremaine 2008). Interestingly, combined with equation (24), the epicycle approximation gives the azimuthal streaming (and hence also the axisymmetric drift) in the equatorial plane as

$$\langle v_\phi \rangle = v_c + \frac{\sigma_R^2}{2v_c} \left( \frac{\partial \ln(\rho\sigma_R^2)}{\partial \ln R} + \frac{\gamma^2 - 1}{\gamma^2} \right). \quad (36)$$

On the other hand, we obtain from equation (20) the following expression for the streaming velocity to leading order in  $\sigma_R/v_c$ :

$$\langle v_\phi \rangle = k v_c + \frac{k \sigma_R^2}{2v_c} \left( \frac{\partial \ln(\rho\sigma_R^2)}{\partial \ln R} \right). \quad (37)$$

Consistency with the epicycle approximation hence requires  $k = 1$



for thin cold disks. The residual difference grows for large  $\sigma_R/v_c$ , but note that in this limit the epicycle approximation becomes inaccurate anyway.

## 4 IMPLEMENTATION DETAILS

### 4.1 Adaptive logarithmic binning

To account for the typical power-law growth of the density towards the center in self-gravitating systems, we generally employ logarithmic grids. For the sake of simplicity, we restrict ourselves to axisymmetric systems in this paper, and also assume mirror symmetry with respect to the  $z = 0$  plane. Adopting cylindrical coordinates, this means we only have to cover the positive quadrant in the  $(R, z)$ -plane. We assume that the mass distribution is fully contained inside a cube of side-length  $2d_{\max}$ , i.e. our mesh needs to cover the region  $0 \leq R < d_{\max}$  and  $0 \leq z < d_{\max}$ . If we use  $N_{\text{bin}} = 2^l$  bins per dimension, and require that the width of the bins grows by a constant factor  $f$  from bin to bin, the borders of the bins can be written as

$$R_i = d_{\text{base}}(f^i - 1), \quad (38)$$

$$z_j = d_{\text{base}}(f^j - 1), \quad (39)$$

with  $i, j \in [0, 1, \dots, N_{\text{bin}}]$ . The bin  $(i, j)$  (with  $0 \leq i, j < N_{\text{bin}}$ ) then covers  $[R_i, R_{i+1}] \times [z_j, z_{j+1}]$  in the  $(R, z)$ -plane and has volume

$$V_{ij} = 2\pi(R_{i+1}^2 - R_i^2)(z_{j+1} - z_j). \quad (40)$$

To cover the full volume,  $d_{\text{base}}$  and  $f$  need to be chosen such that

$$d_{\max} = d_{\text{base}}(f^{N_{\text{bin}}} - 1). \quad (41)$$

This still leaves room for one additional constraint to fully specify the quantities  $d_{\text{base}}$  and  $f$ . We typically address this by requiring that the first bin, bounded by  $R_1 = d_{\text{base}}(f - 1)$ , encloses a small prescribed fraction of the total mass of the system (e.g.  $10^{-6}$ ), such that the central region is still well resolved by the grid.

As we discussed earlier, the objective functions assessing the density response and the initial velocity distribution work best if the spatial bins are chosen such that they contain approximately constant mass. We realize such a scheme by first constructing the mass response on a relatively fine grid, given by the level  $l_{\max}$ . We then recursively construct a set of coarsened meshes on levels  $l_{\max} - 1, l_{\max} - 2, \dots, 1, 0$ , until there is only one cell left covering the whole quadrant. Computing the mass response of one of the grid cells of a coarsened mesh is done recursively by summing over the corresponding four cells in the finer mesh one level higher. Similarly for the velocity dispersion fields.

Evaluating the objective functions then proceeds with a recursive algorithm that walks the tree of nested mesh cells. Beginning at the ‘root node’, a mesh cell is included in the sum if it contains less than a certain threshold mass or if it is already a cell of the finest level. Otherwise, the mesh cell is ‘opened’, and its four daughter cells are considered in turn as candidates for being included in the sum. This procedure automatically selects a close to optimum set of cells of different sizes. Note that the union of the cells that enter the sum form a space-covering tessellation, i.e. each point in the  $(R, z)$ -plane is accounted for exactly once.

In Figure 2 we show an example for the mass response grid of a set of orbits in the  $(R, z)$ -plane for a mesh with  $N_{\text{bin}} = 2^8$  cells per dimension, together with the hierarchy of the next four coarsened representations at higher levels. The final panel on the bottom

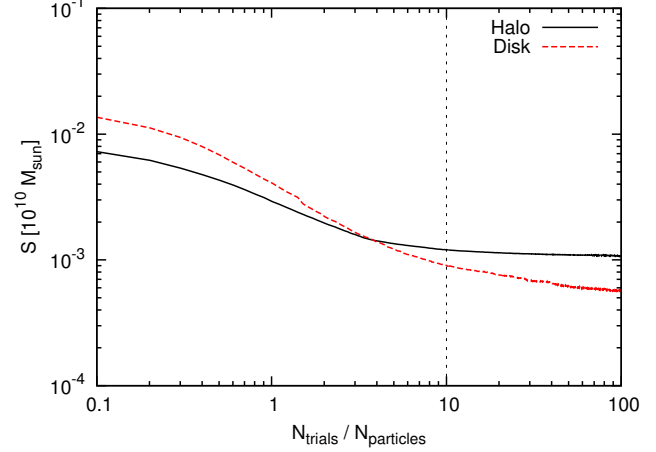


**Figure 3.** Decline of the merit function in a typical optimization run (actually the model D1 from Table 1) as a function of the number of attempted velocity adjustments in units of the particle number of the corresponding component. The solid line shows the result for the dark matter particles, while the dashed lines is for the disk particles.

right shows a mixed image of variable resolution, indicating what is effectively used in the adaptively calculated sum that defines the merit function.

### 4.2 Orbit integration

In order to efficiently and accurately compute orbits of particles for arbitrary mass distributions, we produce a look-up table of the gravitational potential and its derivatives  $\partial\Phi/\partial R$  and  $\partial\Phi/\partial z$  in the positive quadrant of the  $(R, z)$ -plane. Due to the axisymmetry we assume, this is sufficient to obtain the forces and the potential everywhere through a table look-up. We use a fine logarithmic grid in  $R$  and  $z$  and bilinear interpolation for the look-up table.

In order to allow a computation of the forces for arbitrary density distributions without analytic solutions of Poisson’s equation, we numerically evaluate the potential and forces on the fine grid based on randomly sampling the density distribution with a very large number of fiducial particles combined with a calculation of the forces and potentials with a gravitational tree algorithm. This procedure is very flexible and accurate. In order to help reducing noise effects from the sampling to a negligible level, a large number of fiducial points is used, and additionally, we evaluate and average the field at a set of different azimuthal angles.

For the orbit integration of particles, which gives us  $\mathbf{x}_{\text{orbit}}(\hat{\mathbf{x}}_i, \hat{\mathbf{v}}_i, t)$ , we use the leapfrog scheme with adaptive timestep based on the kick-drift-kick formulation. If  $(\mathbf{x}^{(n)}, \mathbf{v}^{(n)})$  denote position and velocity after step  $n$ , then the update to the next step is obtained through

$$\mathbf{v}^{(n+1/2)} = \mathbf{v}^{(n)} + \mathbf{a}^{(n)} \Delta t_n / 2, \quad (42)$$

$$\mathbf{x}^{(n+1)} = \mathbf{x}^{(n)} + \mathbf{v}^{(n+1/2)} \Delta t_n, \quad (43)$$

$$\mathbf{v}^{(n+1)} = \mathbf{v}^{(n+1/2)} + \mathbf{a}^{(n+1)} \Delta t_n / 2. \quad (44)$$

We set the size  $\Delta t_n$  of the timestep of step  $n$  as

$$\Delta t_n = \min \left( \eta_{\text{orbit}} \frac{V_{200}}{|\mathbf{a}^{(n)}|}, \eta_{\text{mesh}} \frac{d_{\text{cell}}^{(n)}}{|\mathbf{v}^{(n)}|} \right), \quad (45)$$

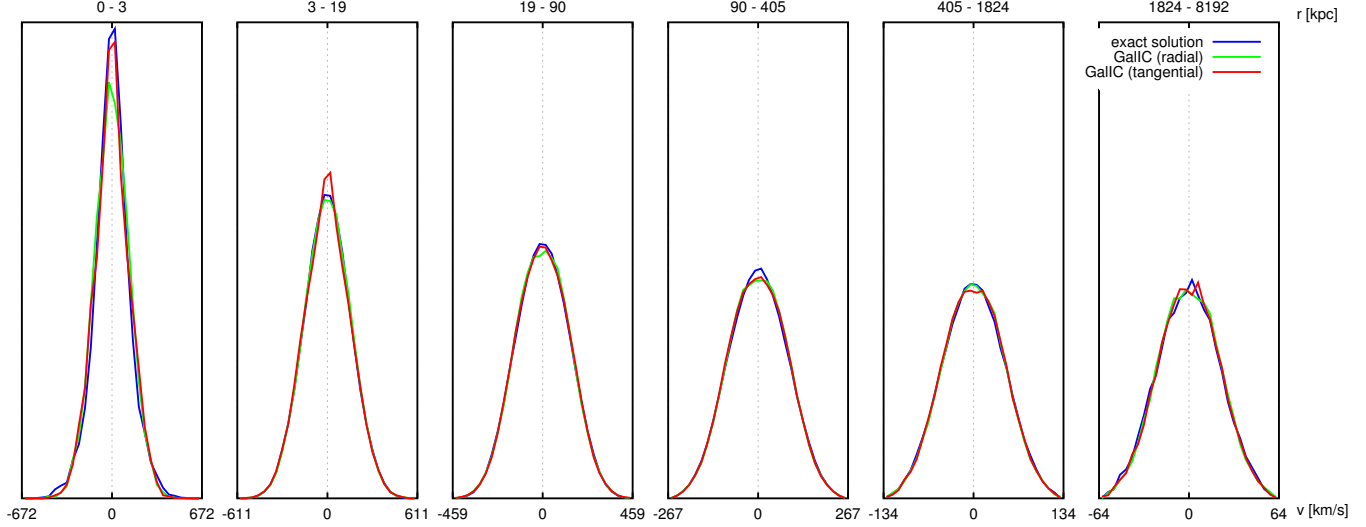


**Figure 4.** Radial and azimuthal velocity distribution functions in different radial shells for the isotropic Hernquist sphere. The blue line show the exact analytic solution. The red and green lines show the constructed solution with our method, separately for azimuthal and radial velocity components. The numbers at the top of each panel indicate the radial range of the measurement.

where  $V_{200}$  is the circular velocity of the halo of the constructed galaxy and  $d_{\text{cell}}^{(n)}$  is the dimension of the mesh cell at the particle’s current location. The dimensionless coefficients  $\eta_{\text{orbit}}$  and  $\eta_{\text{mesh}}$  are meant to ensure an accurate integration of the orbit and a precise accounting of the time spent by the orbit in each of the bins used for recording the density response.

We select the integrated timespan  $T_i$  for each particle individually. To this end we use the circular velocity at the particle’s initial position, and introduce a dimensionless factor  $\eta_{\text{timespan}}$  for scaling the circular orbital time at the local distance. Explicitly, we set

$$T_i = \eta_{\text{timespan}} \frac{2\pi |\hat{\mathbf{x}}_i|}{v_{\text{circ}}(\hat{\mathbf{x}}_i)}, \quad (46)$$

where  $v_{\text{circ}}(\hat{\mathbf{x}}_i) \equiv (|\hat{\mathbf{x}}_i| |\hat{\mathbf{a}}_i(\hat{\mathbf{x}}_i)|)^{1/2}$ . We typically found  $\eta_{\text{timespan}} = 10.0$  to be sufficient, yielding an average number of about 15 orbits for the particles of a typical halo.

### 4.3 Optimization procedure

As discussed earlier, we in principle would like to optimize the particles sequentially. Unfortunately, this immediately poses a serious problem for any efficient parallelization. If we enforce strictly sequential iterative adjustments of the particle velocities (such that a subsequent evaluation of the merit function already takes the effects of a potential change of the previous particle’s velocity fully into account), then the optimization can evidently not be done concurrently for several different particles.

However, we have found that in practice we still obtain good results if we allow a small fraction of all particles to be treated simultaneously, each remaining unaware of the changes in the other particles until these are ‘committed’ at the end of the concurrent phase. With this approach, we can exploit massive parallelism in the optimization procedure (as implemented in our GALIC code).

For definiteness, this practical aspect of our optimization scheme is controlled by a parameter  $f_{\text{opt}}$  which gives the fraction of particle orbits that can be set to new starting velocities without taking note of each other. Our default values for this parameter is  $f_{\text{opt}} = 0.001$ , meaning that our code will process the particles in

batches of size  $f_{\text{opt}} N_{\text{part}}$  particles from a randomly shuffled list of all particles. In each batch, all the trial velocities are drawn and evaluated independently (hence this can be done in parallel), and only at the end the velocity updates are committed to the new global response of the system, affecting the next batch.

When a particle is selected for optimization, we first randomly select one of the three primary coordinate directions, and then replace the corresponding velocity component with one drawn from the corresponding Gaussian distribution. In this way, each of the optimizations effectively couples only to one of the velocity dispersion measures. We found this advantageous also for the following reason. To exclude any possibility that systematic binning effects might prefer orbits that start, for example, with positive  $v_R$  as opposed to negative  $v_R$ , we actually assess orbits by averaging the merit functions for orbits both with  $v_R$  and  $-v_R$  velocities, and likewise for the  $v_z$  velocities. This guarantees symmetry of the resulting velocity distribution functions in these two directions, and in particular,  $\langle v_R \rangle = \langle v_z \rangle = 0$ . However, in the  $\phi$ -direction, this reversal trick is not indicated, both because here the symmetry of the binning procedure excludes the possibility of any such effects by construction (unlike for the  $R$ - and  $z$ -directions), and because in the  $\phi$ -direction orbits with a reversed  $\phi$ -velocity are not necessarily equally probable. We note that to ensure that all particles remain bound, we reject any trial velocity that is larger than  $\eta_{\text{max}} v_{\text{esc}}$ , where  $v_{\text{esc}}$  is the local escape velocity and  $\eta_{\text{max}} = 0.9999$  is a parameter very close to 1.

In Figure 3, we show the decline of the value of the merit function as a function of the number of velocity optimizations that have been attempted by the code, in units of the total particle number, for a typical initial conditions model where the initial velocity guess were computed with the moment-based method. We see that after  $\sim 3$  optimization attempts for each particle, the initial convergence speed slows down significantly, and a stationary state in which no further improvement appears possible is reached after approximately  $\sim 5$  optimizations. We find this is a quite typical behaviour in all of our models. Conservatively, we usually run our models to  $\sim 10$  optimizations per particle.

#### 4.4 Determination of the initial realization

There are only two functions that need to be provided for any desired density distribution that should be treated with our scheme. For each component of the system (i.e. halo, disk and/or bulge), one function needs to return the density of the component at a given point, the other must return a randomly sampled coordinate from the density field, i.e. the probability density of the corresponding point process must be proportional to the density field. Having these functions in hand, we can create the  $\hat{x}_i$  simply by randomly sampling each density component present in the target system. Also, we can create a (large) fiducial set of points for evaluating the force field to arbitrary precision with a tree algorithm. Finally, we can make use of the function returning the continuum density in solving the Jeans equations.

Since in our approach we anyway compute the second moments with the Jeans equations, we may as well initialize initial guesses for the particle velocities  $\hat{v}_i$  by drawing randomly from Gaussian distributions with the correct local dispersions. This corresponds to the frequently invoked approximation of adopting triaxial Gaussians for the local velocity distribution function, and since this is in most cases reasonably close to the correct distribution, it accelerates convergence. The iteration method is then in essence only responsible for determining the higher-order moments of the velocity distribution function.

#### 4.5 Parallelization approach

Our C-code for creating stable initial conditions with the scheme described here, GALIC, has been fully parallelized for distributed memory machines using the message passing interface (MPI). For calculating the gravitational field in the  $(R, z)$ -plane, we let each MPI-task sample particles independently. The resulting particle set is then subjected to a domain decomposition, and a parallel distributed tree algorithm derived from the well-known GADGET simulation code (Springel et al. 2001; Springel 2005) is invoked to compute the force field.

For creating the particles of the actual initial conditions, we again let each MPI-task create a random, disjoint subset of the target particle set for each mass component. Then we let each MPI-task work independently and in parallel on the orbit optimizations associated with one batch of size  $f_{\text{opt}}N_{\text{part}}$ . The results are then interchanged and the sums over the orbit responses are updated accordingly, allowing the next cycle of optimizations to proceed. As a result, the scalability of our code is essentially perfect provided  $f_{\text{opt}}N_{\text{part}}$  is substantially larger than  $N_{\text{CPU}}$ , otherwise work-load imbalances may become substantial as not all tasks could then be expected to have roughly equal amounts of work in each batch.

We have also made use of some of the I/O code from GADGET when writing the final initial conditions to disk. They can be stored in any of the three file formats supported by GADGET (including one in HDF5-format), thereby simplifying the subsequent use of the ICs with this simulation code, or the application of existing file format conversion tools from GADGET's format to other simulation codes. Finally, our use of parallel I/O routines also facilitates the creation of extremely large galaxy models, if desired.

## 5 GALAXY MODELS

The approach outlined above is quite general and can be used with nearly arbitrary axisymmetric density profiles. For definiteness, we

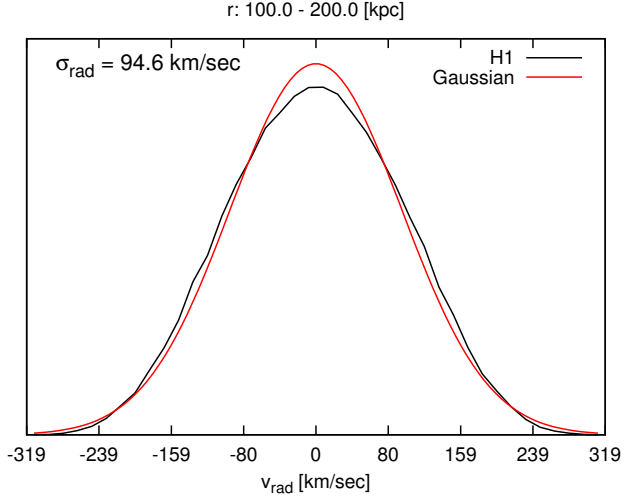


**Figure 5.** Distribution function of the radial velocities in a Hernquist model within a thick radial shell. The black line gives the result of our code for the H1 model, while the red curve is a normal distribution with the same dispersion. The correct platykurtic shape of the distribution function (which is missed in moment-based approaches) is reproduced by our method.

describe in this section a specific set of parameterizations for dark matter halos, stellar disks and stellar bulges, which we shall use in our test galaxy models. These parameterizations follow models widely employed in the literature.

We usually model the dark matter density profile as a spherically symmetric halo with density

$$\rho_{\text{dm}}(r) = \frac{M_{\text{dm}}}{2\pi} \frac{a}{r(r+a)^3}, \quad (47)$$

where  $a$  is the scale factor. Following Springel et al. (2005), we can relate  $a$  to the concentration  $c$  of a corresponding NFW halo of mass  $M_{200} = M_{\text{dm}}$  such that the shape of the density profile in the inner regions is identical. The relation between  $a$  and  $c$  is then given by

$$a = \frac{r_{200}}{c} \sqrt{2[\ln(1+c) - c/(1+c)]}, \quad (48)$$

where  $r_{200}$  and  $M_{200}$  are the virial radius and virial mass of the NFW halo, respectively.

We may also consider axisymmetric dark matter halos with either prolate or oblate distortions. For simplicity, we assume that the isodensity contours of the distorted shape are ellipses, effectively created by linearly distorting the spherical shape along the symmetry axis. If  $s = a/c$  is the (radially constant) stretch factor, and  $a = b$  and  $c$  are the axes of some isodensity ellipsoid, then a prolate halo has  $c/a > 1$  (and hence  $s < 1$ ), while an oblate halo has  $c/a < 1$  (with  $s > 1$ ). We can then define the density profile of the distorted halo as

$$\tilde{\rho}_{\text{dm}}(R, z) \equiv s \rho_{\text{dm}}(\sqrt{R^2 + s^2 z^2}), \quad (49)$$

which leaves the total mass invariant.

For the disk, we adopt in general a model with exponential radial scale length, and a  $\text{sech}^2$ -profile in the vertical direction. More

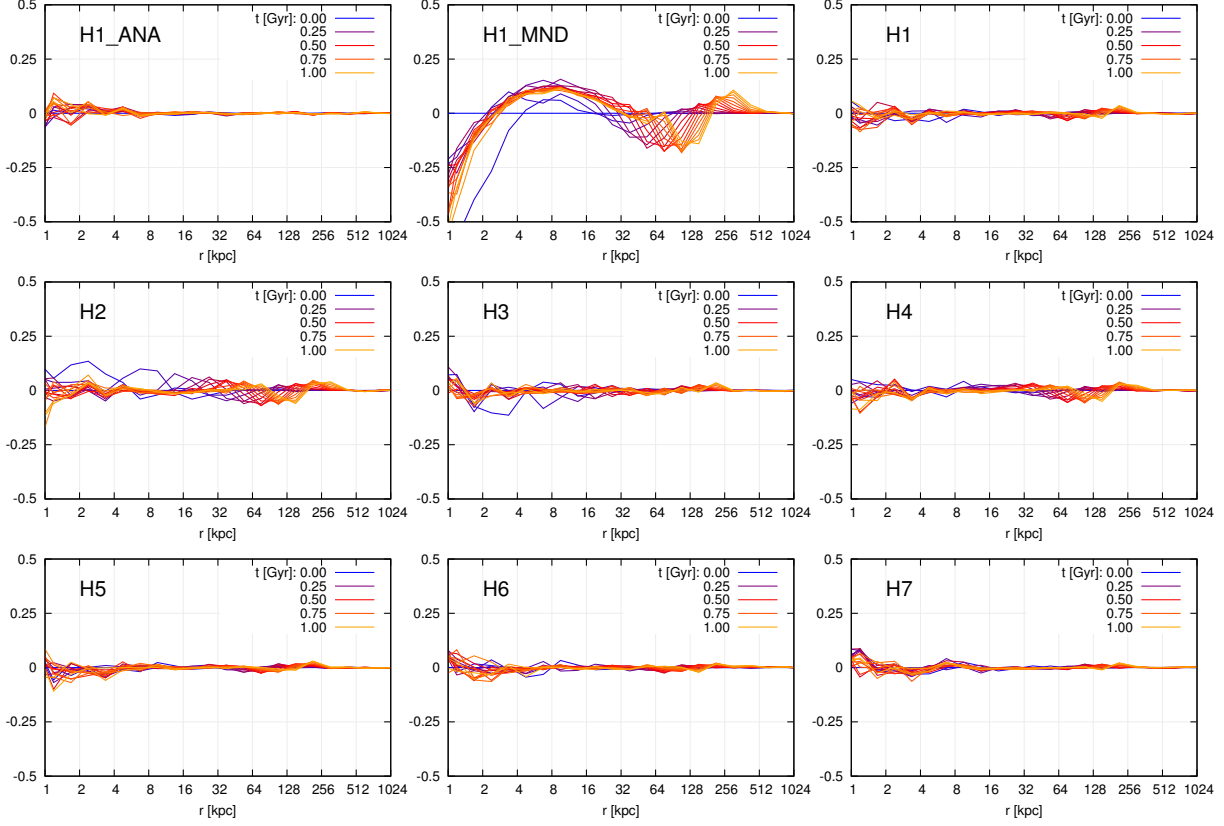


**Figure 6.** Density profile changes of different realizations of our halo-only H-models when evolved in time. The panels show the relative deviation of the spherically averaged density profile from the initial values at different radii and different simulation times. Different line colors mark the different times, as labelled. The top left panel corresponds to initial conditions for the isotropic H1-model realized with the analytic distribution function, while the top middle panel is for the moment-based approach, for comparison. All other results (H1 to H7) are for our new method as implemented in the GALIC code.

specifically, the 3D disk density profile<sup>2</sup> is described by

$$\rho_*(R, z) = \frac{M_*}{4\pi z_0 h^2} \operatorname{sech}^2\left(\frac{z}{z_0}\right) \exp\left(-\frac{R}{h}\right). \quad (50)$$

The disk scale length  $h$  can either be set to a prescribed value, or calculated by assuming that the disk contains a certain fraction of the specific angular momentum of the halo (see, e.g., Mo et al. 1998). We assume a radially constant scale height  $z_0$  of the disk, but this could be easily modified if desired. Usually, we parameterize  $z_0$  in terms of the disk scale length, with typical disks lying in the range  $z_0/h \sim 0.1 - 0.3$ .

Finally, we model a stellar bulge (if present) with a Hernquist halo as well, using the profile

$$\rho_b(r) = \frac{M_b}{2\pi} \frac{b}{r(r+b)^3}. \quad (51)$$

The bulge scale length  $b$  is prescribed through a parameter that gives its size in units of the halo’s scale length.

We specify both the bulge and disk masses as fractions  $m_d$  and  $m_b$  of the total mass, i.e.  $M_d = m_d M_{\text{tot}}$  and  $M_b = m_b M_{\text{tot}}$ . This parameterization has previously been adopted in the study of

<sup>2</sup> We note that equation 10 of Springel et al. (2005) contains a typo in the form of an extraneous factor 1/2 in the argument of the sech-function. All model calculations in that paper have however been done correctly, based on equation 28 of Springel & White (1999), which is what we adopt here too.

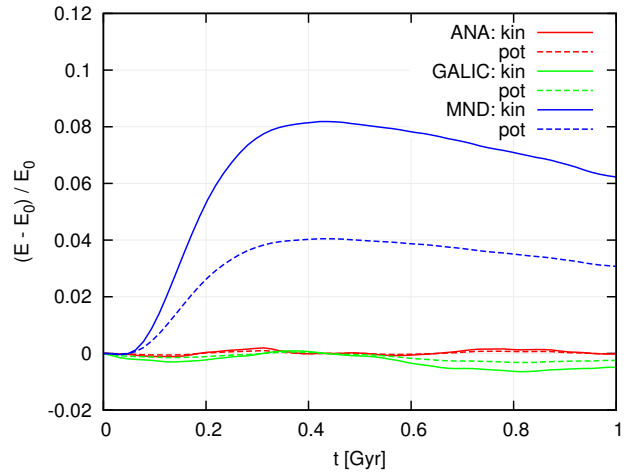


**Figure 7.** Time evolution of the relative change of kinetic and potential energies in the H1 model, for initial conditions realized either through the analytic distribution function (red), through the GALIC code (green), or with a moments based approach (blue).

Mo et al. (1998) on disc structure, as well as in some earlier work on compound disc galaxy models (e.g. Springel & White 1999; Springel et al. 2005).

All the many reasonable combinations of the above compo-

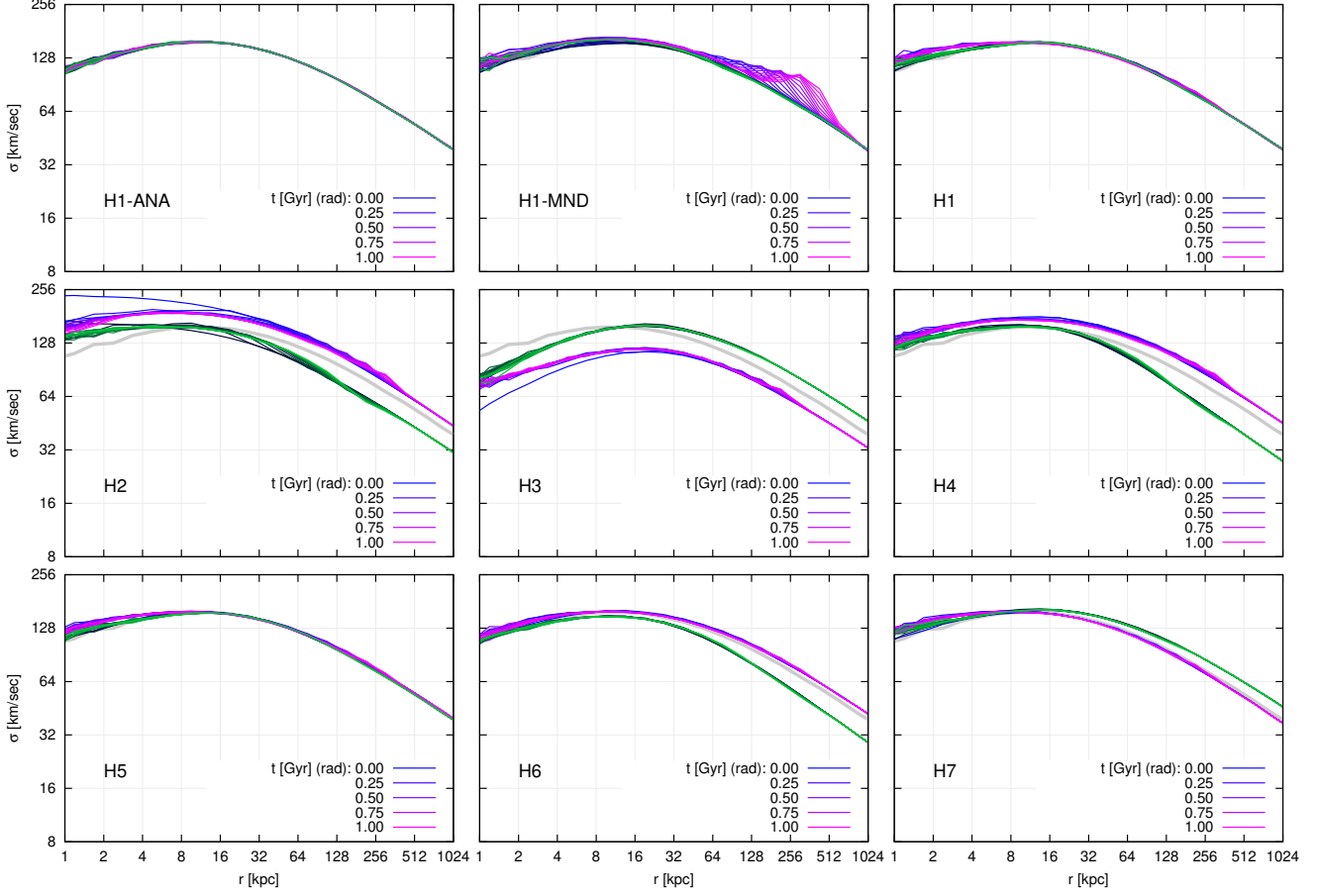


**Figure 8.** Radial and azimuthal velocity dispersion profiles for our models H1 to H7. In each panel, we show the initial conditions produced by GALIC, and the evolved states after different times. The expected profiles based on the Jeans equations are shown underneath. The grey line reproduced the dispersion profile expected for the H1 model, for comparison. In the top row, we also show results for H1 obtained with the analytic distribution function (top left), and with the moment-based method (top, middle).

nents, together with the various velocity structures possible for them, produce a fairly large number of possibilities our code GALIC has to deal with. In particular, requiring that a galaxy model always needs to have a dark matter halo (either of spherical or oblate/prolate shape), that a disk can either be present or absent, and that a bulge is optional but may have different shapes if present (spherical, oblate, or prolate), we already arrive at 12 possible combinations of these three components. Of the corresponding models, only 2 have spherically symmetric potentials (namely either the model with just a spherical halo, or the model with spherical halo and a spherical bulge), allowing ergodic  $f(E)$  distribution functions or  $f(E, |\mathbf{L}|)$  models for them (besides axisymmetric  $f(E, L_z)$  or  $f(E, L_z, I_3)$  distribution functions possible for all the models). Allowing just for different combinations of these extra velocity structures, this means that the 2 density models really correspond to 6 possible variants. Similarly, the other 10 possible density models give rise to 54 possible velocity variants, so that we have of order 60 valid combinations of density model and associated velocity structures. Of course, many of these models really correspond to a continuum of further possibilities once the additional free parameters describing, for example, the degree of net rotation or the radial velocity anisotropy are used.

It is clear that we cannot present exhaustive tests of all these possibilities in this work. Rather, we instead focus on a represen-

tative selection of models which we list in Table 1. This sample of models covers a good fraction of the space of possible model variants of interest, hence our tests should give a good assessment of how well our techniques work in practice. We consider, in particular, models that contain only a dark matter halo (denoted as ‘H1’, ‘H2’, etc.), that feature a pure disk embedded in a halo (labeled ‘D1’, ‘D2’, etc.), that contain a bulge but no disk inside a halo (‘B1’, etc.), and finally, models that feature both a disk and a bulge (‘M1’, ‘M2’, etc.). In each of these four groups, we consider models with a variety of velocity structures, and/or different halo or bulge shapes. Detailed test results for the produced initial conditions will be discussed in the next section.

## 6 TEST RESULTS

### 6.1 Models with a single halo component

The simplest of our models is ‘H1’, featuring a Hernquist dark matter halo with an isotropic velocity distribution. For definiteness, we adopt  $v_{200} = 200 \text{ km s}^{-1}$  and  $c = 10$  to set the total mass and concentration of the halo, and we use  $N = 10^6$  particles in order to have enough sampling points for a reliable measurement of the produced velocity distribution function.



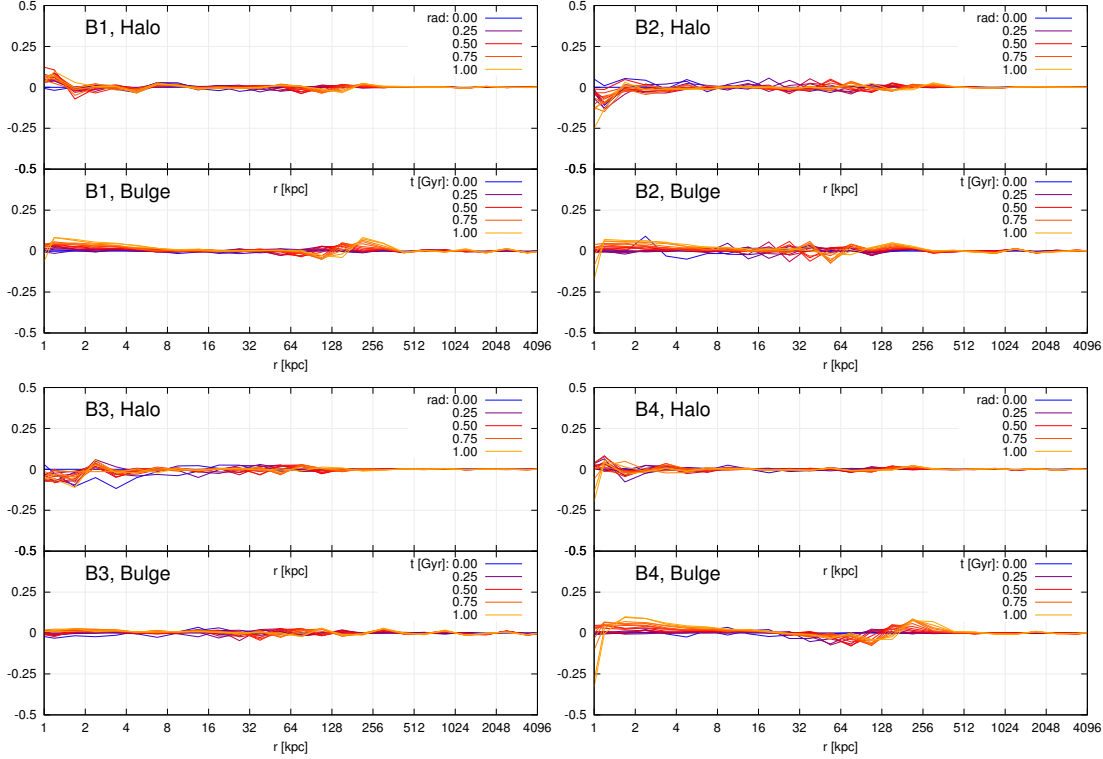


**Figure 10.** Density profiles changes of different bulge models (B-models in Table 1) when evolved in time. For each of the four models, two panels are given that show the relative deviation of the spherically averaged density profile of halo and bulge components relative to the initial values, as a function of radius and for different simulation times. Different line colors mark the different times, as labelled.

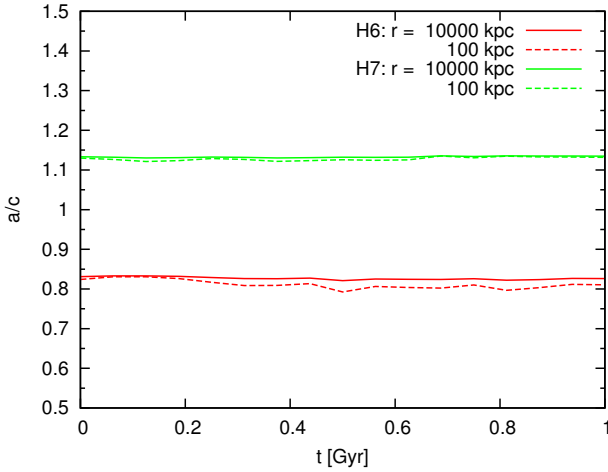


**Figure 9.** Halo shapes of models H6 and H7 as a function of evolution time. We show the ratios of the principal eigenvalues of the moment-of-inertia tensor at two different radii as a function of time. The values reproduce the intended shapes according to Table 1, and are constant in time.

In Figure 4, we show radial and azimuthal velocity distribution functions measured from the ICs produced by our code for this classic Hernquist model, where the analytic distribution function is known analytically. We measure the distribution function in a set of 6 radial shells, as labelled in the different panels. In each panel, we show the analytic distribution function in blue, and the one produced by the GALIC code in red (azimuthal direction) and

green (radial direction), respectively. We can nicely see from the figure that the model calculated by GALIC reproduces the expected distribution function rather well in all radial shells, without any significant difference. In particular, note that the model produces the platykurtic nature of the velocity distribution of the Hernquist sphere, which directly shows the presence of higher-order moments that are missed by simpler moment-based methods but are captured by our new approach. This is seen explicitly in Figure 5, where we compare the shape of the produced radial velocity distribution function to a Gaussian with the same dispersion.

The most important critical test of a method's ability to create initial conditions in equilibrium is however to check the stability of the ICs in a self-consistent simulation under its own self-gravity. To this end, we use the GADGET N-body code, with force accuracy and time integration parameters set conservatively such that energy conservation is excellent. To control discreteness effects in the potential we set the gravitational softening length to a value of 0.05 kpc. In this way we make sure that any secular evolution that is seen really reflects imperfections of the ICs rather than being influenced also by N-body integration errors or two-body relaxation.

Figure 6 shows the relative deviation of the spherically averaged density profile from the initial values at different radii and different simulation times, for our H-models. Different line colors mark the different times, as labelled. We have here restricted the simulation time to 1 Gyr, but note that nothing qualitatively changes if this is expanded to 10 Gyrs, significantly longer than the dynamical time of the galaxy model. Let us first focus on a comparison of runs for three different initial conditions constructed for H1, the isotropic Hernquist model. The simulation starting from ICs created with the analytic distribution function is shown in the top left

panel, the top right panel shows our GALIC technique, and the top middle panels gives the moment-based method (here realized with the MAKENEWDISK code described in Springel et al. 2005). As can be seen, our result (top right panel) is nearly indistinguishable from the analytic initial conditions. There is a hint of some small deviations standing out of the noise compared with the analytic solution, but this is very small if real at all. In contrast, for the moment-based method we see a prominent perturbation propagating outwards, irreversibly changing the mass distribution of the system as it relaxes to a new equilibrium state.

Another view of this difference in the dynamical evolutions of these three simulations is given in Figure 7, where we compare the relative changes of the kinetic and potential energies of the three runs as a function of time. We can see that both the  $N$ -body realization drawn from the analytic Hernquist distribution function and the GALIC result show essentially stationary energies over the simulation, as expected from a virialized system in equilibrium. In contrast, the moment-based approach shows a rapid evolution in the energies in the first  $\sim 300$  Myr, and only then settles into a stationary state. Note that in this initial phase, the central potential fluctuates, allowing individual particles to change their energies and the system to relax to a new equilibrium.

We now turn to considerably more demanding models that have an anisotropic, but still spherically symmetric velocity structure. These are models H2, H3, and H4, characterized by asymmetry parameters  $\beta = -1$  (for H2) and  $\beta = 0.5$  (for H3), corresponding to the cases  $\sigma_r^2 = \sigma_\theta^2/2$  and  $\sigma_r^2 = 2\sigma_\theta^2$ , respectively. The model H4 adopts a radially varying profile  $\beta(r)$  as suggested by cosmological simulations.

In Figure 8, we show radial profiles of the radial and azimuthal velocity dispersion profiles for initial conditions produced by GALIC for these 4 cases (and for completeness also for all other H-models), both at the initial time and after different times of evolution. For reference, we also include in the figure panels the result for H1 (top left panel) as a grey line, which is the isotropic  $\beta = 0$  case. We see that the initial conditions code manages to accurately impose the desired velocity anisotropy at the initial time. Upon time evolution, these velocity dispersion profiles are quite well maintained, but not perfectly in the very central regions for models H2, and to lesser extent, H3. While these two models still manage to maintain a directional difference in the velocity dispersions in the innermost halo even after 1 Gyr of evolution, the initial profile is not fully retained in the very central region. Overall, we consider these results however still to be quite good.

We note however that the density profiles of these anisotropic models are accurately retained even in the centres in these anisotropic cases. Some of the panels of Figure 6 report the density variations of the anisotropic models H2-H4 upon time evolving their ICs. The relative fluctuations of the density profiles are very small, consistent with the findings for the simple H1 model. Note that in Fig. 6 we also include results for the models H5, H6, and H7. These latter three models now feature an axisymmetric assumption for their velocity structure. H5 is actually slowly rotating, whereas H6 and H7 have prolate or oblate shape distortions, respectively. The absence of any significant time evolution in the spherically averaged density profiles shown in Fig. 6 indicates that these models are also rather robust and in good equilibrium.

This is also confirmed by a look at their velocity dispersion profiles shown in Figure 8, and a direct analysis of the halos shapes of models H6 and H7 at the final times. Simple measurements of the eigenvalues of their moment of inertia tensors as a function of time (see Figure 9) confirm that the imposed halo shapes are accu-

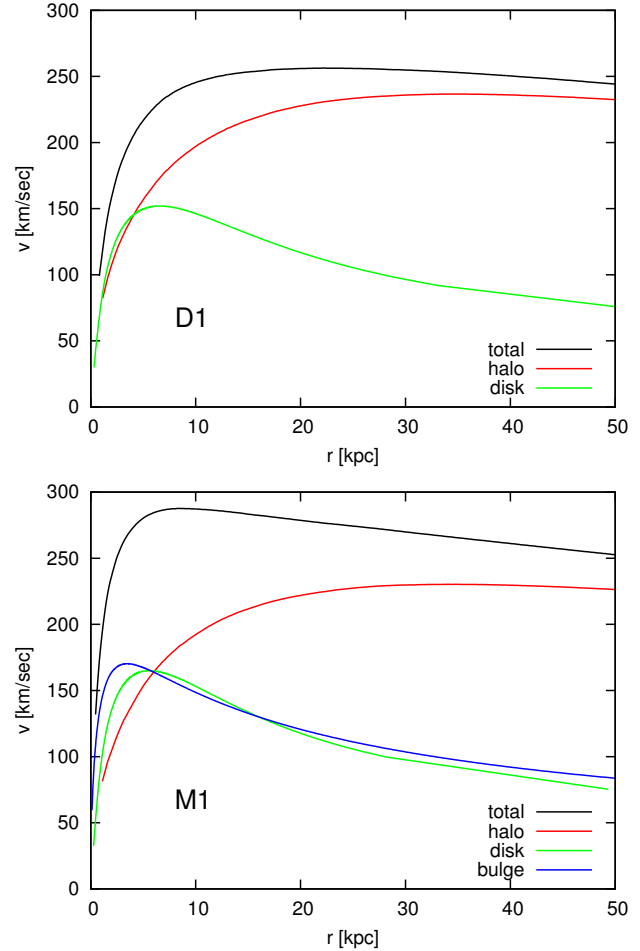


**Figure 11.** Rotation curves of the different mass components in our D-models (top panel) which contain only a dark matter halo and a stellar disk, and our M-models (bottom panel) which in addition contain a central bulge.

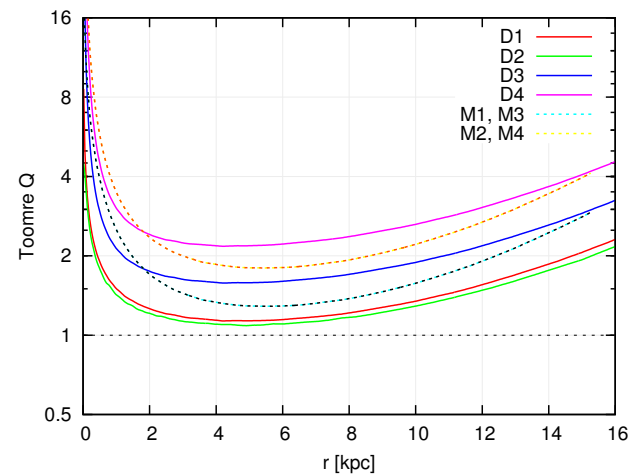


**Figure 12.** Stability against axisymmetric perturbations as expressed through the Toomre  $Q$ -parameter, for different D- and M-models.

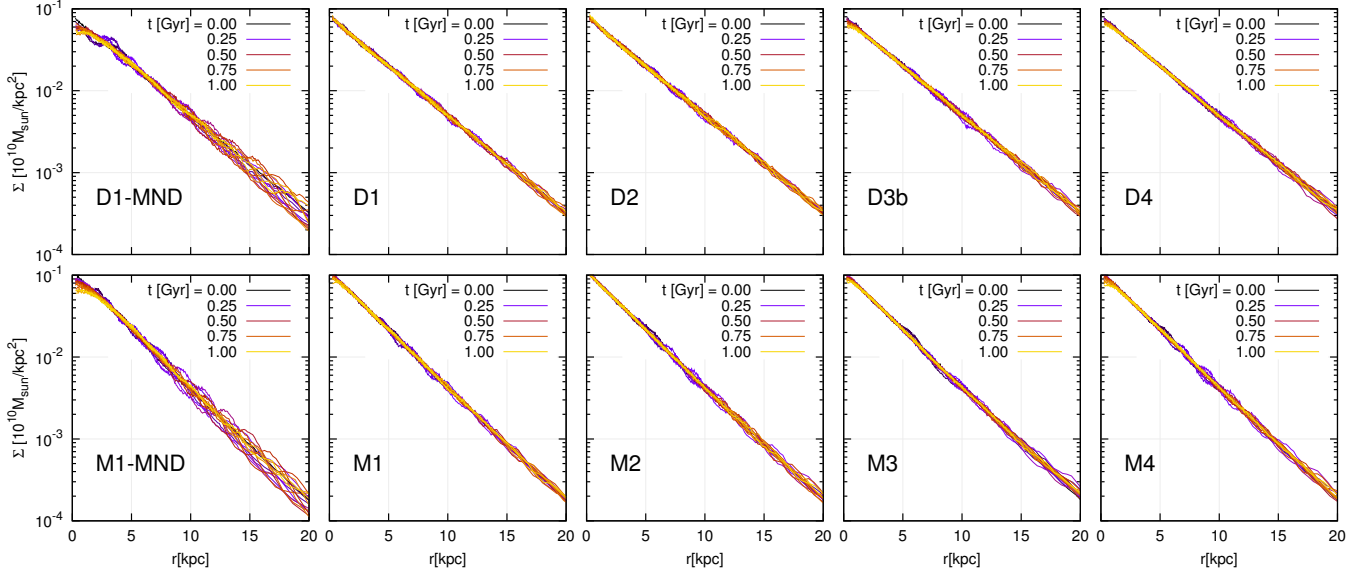


**Figure 13.** Radial surface density profiles of the stellar disk component under time evolution, for D1-D4 (top row), and M1-M4 (bottom row). The left column shows the D1 and M1 models again, but this time for initial conditions produced with the moment-based approach implemented in MAKENEWDISK.

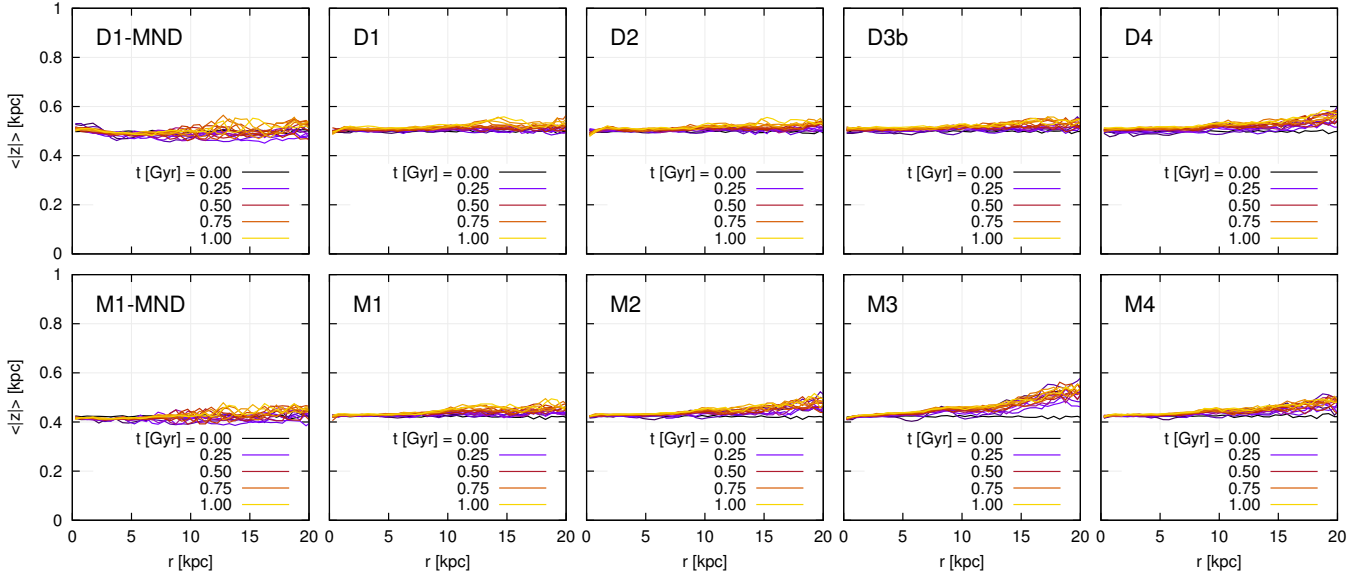


**Figure 14.** Vertical disk height as a function of radius at different times when our disk models are evolved in time, for the D1-D4 models (top row), and the M1-M4 models (bottom row). In the left column, we show for comparison the corresponding results when the initial conditions for D1 and M1 are constructed with a moment-based approach.

rately retained over time. We also note that the time evolution of the kinetic and potential energies (not shown) confirms that the models are in good equilibrium.

## 6.2 Systems with a bulge and a halo

Next, we consider models that are slightly more complicated and feature two different mass components of very different spatial extent, a Hernquist halo with an embedded, much smaller stellar bulge, also modelled with a Hernquist profile. Our model B1 simply consists of two ergodic systems nested into each other. B2 varies that

by invoking different velocity anisotropies for halo and bulge, with a preference for radial orbits in the halo and tangential ones in the bulge. Finally, B3 and B4 test different shape distortions for halo and bulge, under the assumption of an axisymmetric velocity structure and no net rotation.

Figure 10 shows the changes in the radially averaged density profiles of these systems when they are evolved in time, separately for the stellar bulge and the dark matter components. The stability appears to be excellent in most cases, something that is also confirmed by other measures, such as the time evolution of kinetic and potential energies. Only the B2 model performs slightly worse, an



outcome that we blame on the dominance of radial orbits in the dark matter component of this model even in the very centre (similar as in H2), and some of these orbits can be affected by the radial orbit instability (Buyle et al. 2007).

### 6.3 Systems with a halo, a disk, and an (optional) bulge

We now turn to the much more challenging case of models containing a thin stellar disk. In Figure 11, we show the rotation curves of our models containing just a halo and a disk (D-models, top panel), and those of our models containing in addition a bulge as well (M-models, bottom panel). In the innermost regions, the disk dominates slightly over the spheroidal halo in the D-models. The specific parameters chosen for the D-models are  $m_d = 0.035$  and  $\lambda = 0.035$ , and the M-models contain additionally a bulge with  $m_b = 0.05$  and a scale length set to a tenth of that of the halo. We note that these choices are somewhat arbitrary and not meant to represent a specific system such as the Milky Way; our methods work with similar quality when the parameters are varied over a plausible range.

Interestingly, depending on what assumptions we make about the velocity structure of the disk systems, the expected stability with respect to axisymmetric perturbations can be quite different. In Figure 12, we show Toomre's  $Q$ -parameter for the disk models D1 to D4, as well as for our M-models. As we see, D1 actually nearly straddles the stability boundary at  $Q = 1$ , and can hence be expected to be somewhat more prone to axisymmetric perturbations than D3, were  $Q$  is boosted thanks to a higher radial velocity dispersion.

In Figure 13, we show the time evolution of the azimuthally averaged projected disk surface density profiles, for models D1-D4, and for M1-M4. We can see that all models are reassuringly stable. The improvement compared with moment-based methods such as that implemented the MAKENEWDISK code can perhaps be best appreciated by comparing to the results for this method, which are given in the leftmost panels of Fig. 13 for models D1 and M1.

Finally, a complementary view of the disk stability is obtained by considering the time evolution of the vertical density structure of the disks, which is shown in Figure 14. Again, the models D1-D4 and M1-M4 are seen to retain their disk density structure accurately, relatively independent of the different variants of halo and bulge shapes, and the different degrees of rotation that we tried. Only M3 performs noticeably worse than the other models in the outer disk. When we compare the D1 and M1 models to corresponding realizations obtained with the moment based approach (left most panels in the figure), there is a clear improvement.

### 6.4 Dependence on nuisance parameters

Our iterative method for finding equilibrium galaxy models with the GALIC code involves several free parameters, for example the fraction of particles that is allowed to be concurrently optimized, the number of optimization cycles before a randomization is carried out, the resolution of the density response grid, the length of time over which orbits are integrated, and a few more minor ones.

We have carefully tested whether our results depend significantly on the settings of any of these parameters. This is fortunately not the case. We find that our results are rather robust when any of these nuisance parameters is changed around our default settings. As a case in point, we show in Figure 15 an explicit test for the number of orbits that are integrated, comparing results produced for the M1 model where this parameter has been lowered by a factor of 2, or increased by a factor of 2, compared with our default

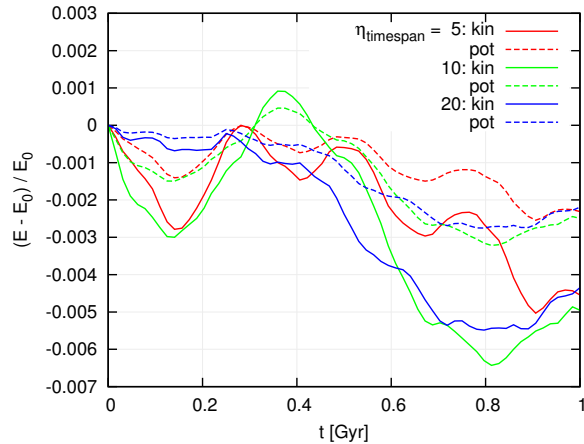


**Figure 15.** Test of the dependence of our results on the integration time of particle orbits. We show the relative changes in potential and kinetic energies when evolving initial conditions constructed with integration times lowered or increased by factors of two relative to our default value. The particular system used here is M1, but similar results are found for other models and other changes of numerical parameters in our code.

choice. Reassuringly, we see that the density deviations occurring in time evolutions of the produced ICs are of very similar magnitude, i.e. their quality appears indistinguishable.

We also find that that the grid resolution used for recording density and velocity dispersion responses plays only a negligible role for the results, provided the finest possible level is not overly coarse. This can be understood as a result of our adaptive binning prescription. Potentially more important may be the value of the number of particles required in a cell before it may be split up in finer cells. But we have also found here that varying this parameter over a significant range does not change the results appreciably. Finally, the last free parameter that we have extensively tested is the integration accuracy of the orbits. Here our typical relative energy errors for the integration of individual orbits are below  $10^{-3}$ , already suggesting that this should be good enough and not introduce any significant errors into the results. Indeed, investing more computational effort and lowering the integration errors through finer timestepping does not change our results in any significant way.

## 7 DISCUSSION AND CONCLUSIONS

In this paper, we introduced a new iterative method for constructing equilibrium  $N$ -body galaxy models. The principle advantage of our method is that it can produce  $N$ -body systems that are essentially in exact equilibrium for rather general density distributions, making the method ideal for studies of galaxy dynamics and numerical experiments with isolated or colliding galaxies. Compared to alternative schemes like the Schwarzschild method, our approach eliminates restrictions arising from a finite orbit library or from required regularization schemes. Also, our method allows a natural inclusion of simulation aspects like the need for a gravitational softening.

The test results we have analyzed show a considerable improvement of the quality of the created initial conditions compared to existing codes such as the moment-based MAKENEWDISK, a technique that has been used in numerous studies over recent years. This is possible thanks to the absence of any assumptions in our approach with respect to the importance of higher-order moments of the velocity distribution function. The main disadvantage of our

method lies in its higher computational cost compared to moment-based approaches. However, thanks to the scalable parallelization implemented of our code, this should not be a serious restriction in practice. For example it took about 5 hours on 96 AMD-6174 cores (2.2 GHz) to compute high-quality solutions for our most complicated models M1-4, while for the one component models it took only 1 hour. And since poor ICs may also impact any further scientific investigation, the additional CPU effort invested for better ICs should in many cases be well worth the effort.

Finally, we also note that numerous optimizations in our code could well be made to reduce its CPU time consumption. For example, the time to full convergence for a system with large  $N$  may be reduced considerably by first treating a smaller subsample of the particles with correspondingly higher mass. Once this system has fully converged, one could then create the large target realization from it through bootstrap sampling, followed by briefly relaxing the big system to the final equilibrium.

In future work, it might be interesting to extend our approach to genuinely triaxial systems, which are of course considerably more challenging than the axisymmetric case considered here. One could even include additional phenomena such as figure rotation. An important challenge is here to suitably store the density response grid. Here, our approach, which only requires essentially one such response grid should be considerably less restrictive than Schwarzschild's method because the requirement to store a huge orbit library is avoided. In the meantime, we publicly release our GALIC code (<http://www.h-its.org/tap/galic>), hoping that it proves useful for future N-body studies in galactic dynamics.

## ACKNOWLEDGEMENTS

We thank the referee for constructive comments that helped to improve the paper. D.Y. and V.S. acknowledge support by the DFG Research Centre SFB-881 'The Milky Way System' through project A6. This work has also been supported by the European Research Council under ERC-StG grant EXAGAL-308037 and by the Klaus Tschira Foundation.

## REFERENCES

- Athanassoula E., Misiriotis A., 2002, *MNRAS*, 330, 35  
 Barnes J. E., Hernquist L., 1992, *ARA&A*, 30, 705  
 Binney J., Burnett B., Kordopatis G., Steinmetz M., Gilmore G., Bienayme O., Bland-Hawthorn J., Famaey B., Grebel E. K., Helmi A., Navarro J., Parker Q., Reid W. A., Seabroke G., Watson F., Williams M. E. K., Wyse R. F. G., Zwitter T., 2014, *MNRAS*, 439, 1231  
 Binney J., Merrifield M., 1998, *Galactic Astronomy*  
 Binney J., Tremaine S., 2008, *Galactic Dynamics: Second Edition*. Princeton University Press  
 Buyle P., van Hese E., de Rijcke S., Dejonghe H., 2007, *MNRAS*, 375, 1157  
 Cretton N., de Zeeuw P. T., van der Marel R. P., Rix H.-W., 1999, *ApJS*, 124, 383  
 Dehnen W., 2009, *MNRAS*, 395, 1079  
 D'Onghia E., Springel V., Hernquist L., Keres D., 2010, *ApJ*, 709, 1138  
 D'Onghia E., Vogelsberger M., Hernquist L., 2013, *ApJ*, 766, 34  
 Hansen S. H., Moore B., 2006, *New Astronomy*, 11, 333  
 Hernquist L., 1990, *ApJ*, 356, 359  
 Hernquist L., 1993, *ApJS*, 86, 389  
 Hernquist L., Mihos J. C., 1995, *ApJ*, 448, 41  
 Holley-Bockelmann K., Mihos J. C., Sigurdsson S., Hernquist L., 2001, *ApJ*, 549, 862  
 Jaffe W., 1983, *MNRAS*, 202, 995  
 Jalali M. A., Tremaine S., 2011, *MNRAS*, 410, 2003  
 Kazantzidis S., Bullock J. S., Zentner A. R., Kravtsov A. V., Moustakas L. A., 2008, *ApJ*, 688, 254  
 Kuijken K., Dubinski J., 1995, *MNRAS*, 277, 1341  
 Merritt D., 1985, *MNRAS*, 214, 25P  
 Mo H. J., Mao S., White S. D. M., 1998, *MNRAS*, 295, 319  
 Navarro J. F., Frenk C. S., White S. D. M., 1997, *ApJ*, 490, 493  
 Osipkov L. P., 1979, *Soviet Astronomy Letters*, 5, 42  
 Rodionov S. A., Athanassoula E., Sotnikova N. Y., 2009, *MNRAS*, 392, 904  
 Satoh C., 1980, *PASJ*, 32, 41  
 Schwarzschild M., 1979, *ApJ*, 232, 236  
 Sellwood J. A., Binney J. J., 2002, *MNRAS*, 336, 785  
 Siebert A., Bienaymé O., Binney J., Bland-Hawthorn J., Campbell R., Freeman K. C., Gibson B. K., Gilmore G., Grebel E. K., Helmi A., Munari U., Navarro J. F., 2008, *MNRAS*, 391, 793  
 Springel V., 2005, *MNRAS*, 364, 1105  
 Springel V., Di Matteo T., Hernquist L., 2005, *MNRAS*, 361, 776  
 Springel V., White S. D. M., 1999, *MNRAS*, 307, 162  
 Springel V., Yoshida N., White S. D. M., 2001, *New Astronomy*, 6, 79  
 Syer D., Tremaine S., 1996, *MNRAS*, 282, 223  
 van den Bosch R. C. E., Gebhardt K., Gültekin K., van de Ven G., van der Wel A., Walsh J. L., 2012, *Nature*, 491, 729  
 Vandervoort P. O., 1984, *ApJ*, 287, 475  
 Widrow L. M., Dubinski J., 2005, *ApJ*, 631, 838